The Nuclear Equation of State and Neutron Star Masses

James M. Lattimer

Department of Physics and Astronomy, Stony Brook University, Stony Brook, New York
11794-3800; email: lattimer@astro.sunysb.edu

Keywords

neutron stars, dense matter equation of state, nuclear symmetry energy

Abstract

Neutron stars are valuable laboratories for the study of dense matter. Recent observations have uncovered both massive and low-mass neutron stars and have also set constraints on neutron star radii. The largest mass measurements are powerfully influencing the high-density equation of state because of the existence of the neutron star maximum mass. The smallest mass measurements, and the distributions of masses, have implications for the progenitors and formation mechanisms of neutron stars. The ensemble of mass and radius observations can realistically restrict the properties of dense matter and, in particular, the behavior of the nuclear symmetry energy near the nuclear saturation density. Simultaneously, various nuclear experiments are progressively restricting the ranges of parameters describing the symmetry properties of the nuclear equation of state. In addition, new theoretical studies of pure neutron matter are providing insights. These observational, experimental, and theoretical constraints of dense matter, when combined, are now revealing a remarkable convergence.

Contents

1. INTRODUCTION

Neutron stars contain matter with the highest densities in the observable universe. As such, they are valuable laboratories for the study of dense matter. They are so compact that general relativity is essential to their structures; indeed, the existence of a maximum neutron star mass is a manifestation of general relativity. Their compactness, however, makes them challenging to study. The vast majority of neutron stars are observed as pulsars (1), and nearly 2,000 have been detected (see **http://www.atnf.csiro.au/research/pulsar/psrcat** and **http://www3.mpifr-bonn.mpg.de/old_pifr/div/pulsar/data/archive.html** for pulsar databases). Currently, however, only a few aspects of neutron stars can be inferred from pulsar observations, such as masses, spin rates, rough ages, and magnetic field strengths, although outstanding accuracy in mass measurements (<0.1%) is sometimes achieved (2, 3).

Other crucial properties that are important for understanding the structure and evolution of neutron stars, such as radii and surface temperatures, can be estimated in a few cases from optical and X-ray observations of cooling neutron stars as well as from X-ray bursts and flares occurring on neutron star surfaces (see Section 4). One newly formed neutron star was observed in neutrinos (4) in the aftermath of the supernova SN 1987A, but only the roughest estimates for its mass, binding energy, and radius were revealed (5). A galactic supernova today would result in the detection of perhaps hundreds of times more neutrinos, which should allow for more precise estimates. In the near future, observations of gravitational waves containing mass and radius information (6) from merging binaries containing neutron stars are expected. Unfortunately, at present, precise measurements of both the mass and the radius of individual neutron stars do not exist. Current goals are to combine available observations to deduce the underlying equation of state (EOS) of dense matter, the subject of this review, and to infer their internal composition from their cooling histories (7, 8).

At the same time, ongoing laboratory measurements of nuclear properties and theoretical studies of pure neutron matter are limiting the properties of neutron star matter near the saturation density (usually expressed as baryon density, $n_s \simeq 0.16$ baryons fm^{-3}; mass density, $\rho_s \simeq 2.7 \times 10^{14}$ g cm^{-3}; or energy density, $\varepsilon_s \simeq 150$ MeV fm^{-3}). In this review, we show that estimates of the EOS from astrophysical observations are converging with those from laboratory studies. This development is important because it means that the range of EOS properties that needs to be explored during simulations of supernovae and neutron star mergers is shrinking.

In Section 2, we present the basics of neutron star structure, and we explore the limits with the aid of the maximally compact EOS. In Section 3, we present techniques for extracting the masses of neutron stars in binary systems and tabulate the mass measurements. We summarize the results for the maximum and minimum neutron star masses and the distribution of neutron star masses. In Section 4, we describe other observations in which simultaneous mass and radius information can be obtained, and in Section 5 we discuss the computation of the universal mass-radius and pressure-density relations from observations. Finally, in Section 6 we summarize the available laboratory nuclear physics constraints, as well as recent theoretical studies of pure neutron matter.

2. NEUTRON STAR STRUCTURE AND THE MAXIMALLY COMPACT EQUATION OF STATE

2.1. The Mass-Radius Relation

At very low temperatures, and for matter in weak-interaction equilibrium, the only aspect of the EOS that is relevant for the global structure of neutron stars is the pressure–energy density relation. The composition of matter, usually parameterized by the number of electrons per baryon Y_e, is implicitly determined at each density n by minimizing the energy density ε, which results in the condition of β equilibrium,

$$\left(\frac{\partial \varepsilon/n}{\partial Y_e}\right)_n = \mu_e + \mu_p - \mu_n = 0,$$

1.

where the chemical potentials of neutrons, protons and electrons are μ_n, μ_p, and μ_e, respectively. In this case, the general relativistic equations of hydrostatic equilibrium (9) are expressed by

$$\frac{dp}{dr} = -\frac{G}{c^2}\frac{(p+\varepsilon)(m+4\pi r^3 p/c^2)}{r(r-2Gm/c^2)},$$
$$\frac{dm}{dr} = 4\pi r^2 \frac{\varepsilon}{c^2},$$

2.

where p is the pressure, m is the enclosed mass, and r is the radius; n is related to ϵ and p by $nd\epsilon/dn = \epsilon + p$. Beginning from the center, where $m = r = 0$, $p = p_c$, and $\varepsilon = \varepsilon_c$, these equations are integrated to the surface, where $p = p_{\mathrm{surf}} = 0$, $r = R$, and $m = M$. For hadronic EOSs, $\varepsilon_{\mathrm{surf}} = 0$, but this is not the case for pure strange quark matter (SQM) stars, for which the energy density remains finite. **Figure 1** shows these features for schematic hadronic and pure SQM EOSs. The hadronic EOS consists of two polytropes (i.e., $p = Kn^\gamma$); the exponents $\gamma_1 = 4/3$ and $\gamma_2 = 3$ are joined at the transition pressure $p_t = p_s/8$, where $p_s = 2.5$ MeV fm^{-3}. The transition occurs at baryon density $n_s/2$. The SQM EOS is the simple MIT bag model, $\varepsilon = 4B + 3p$ (10), where the bag constant is chosen to be $B = 3\varepsilon_s/8$.

In the Newtonian limit, the equations of hydrostatic equilibrium are $dp/dr = -G\rho m/r^2$ and $dm/dr = 4\pi \rho r^2$, where $\rho = nm_b$. Dimensional analysis for a polytropic EOS results in scalings between the radius R and total mass M:

$$R \propto K^{1/(3\gamma-4)}M^{(\gamma-2)/(3\gamma-4)}; \quad M \propto K^{1/(2-\gamma)}R^{(3\gamma-4)/(\gamma-2)}.$$
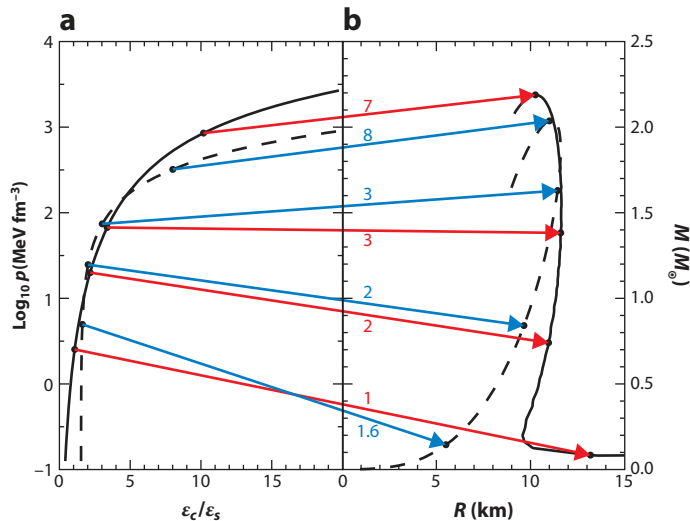
3.

Figure 1

(*a*) Schematic hadronic (*solid curves*) and pure strange quark matter (*dashed curves*) equations of state. (*b*) The corresponding $M-R$ relations. Arrows connect specific central energy density and pressure values with their corresponding (M, R) points. The numbers labeling hadronic arrows denote central baryon densities n_c/n_s, and those labeling strange quark matter arrows indicate $\varepsilon_c/\varepsilon_s$. The uppermost arrows in each case mark the maximum mass configurations.

For the case in which $\gamma \sim 4/3$, valid for hadronic matter at densities below $\rho_s/3$ (where the pressure is dominated by relativistic degenerate electrons), $M \propto K^{3/2} R^0$, which is independent of radius. At extremely large radii ($R \gtrsim 300$ km), the mass starts to increase as configurations approach the white dwarf (WD) range (such configurations have much larger proton concentrations). Thus, there is a minimum stable mass for neutron stars, which is approximately $0.09\, M_\odot$ (11), when $R \sim 200$–300 km.

For higher densities, in the range $\varepsilon_s - 3\varepsilon_s$, the typical behavior of hadronic EOSs is $\gamma \sim 2$ (**Figure 2**). In this case, the scaling becomes $R \propto K^{1/2} M^0$, and the radii are nearly independent of mass.

In the hadronic case, both asymptotic behaviors are apparent in **Figure 1**, and the transition between them occurs near $n_c \sim n_s$. At high densities, general relativity becomes dominant and causes the formation of a maximum mass. In the case of SQM stars at low densities, the large value of B essentially results in $\gamma \to \infty$ so that $R \propto K^0 M^{1/3}$, a behavior also shown in **Figure 1**.

An interesting feature of **Figure 1** is that the SQM and hadronic EOSs predict very similar $M-R$ trajectories in the range $1.5 < M/M_\odot < 2$. It would clearly be difficult, on the basis of observational $M-R$ data alone, to distinguish these trajectories. This observation suggests that other data, such as neutron star cooling information (12), will be necessary to confirm the existence of SQM stars.

It is useful to display $M-R$ curves for various realistic EOSs, as demonstrated in **Figure 3** for several of the EOSs plotted in **Figure 2**. Those hadronic EOSs with extreme softening (due to a kaon or pion condensate, high abundances of hyperons, or a low-density quark-hadron phase transition) do not have pronounced vertical segments, but they also do not allow the existence of a $2\text{-}M_\odot$ neutron star (see Section 3) and, therefore, cannot be physical. The $M-R$ curves that have attained sufficient mass have vertical segments with radii varying from 10 to 16 km (the extreme
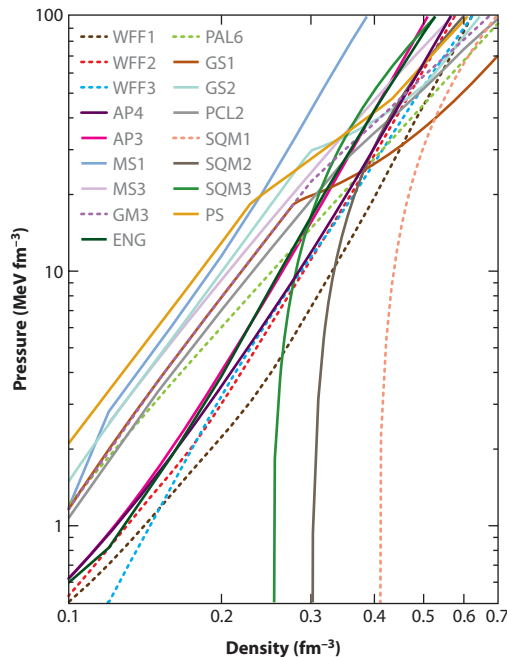
Figure 2

Representative hadronic and strange quark matter equations of state (EOSs). The mean exponent $\gamma = d \ln p / d \ln n \simeq 2$ holds for hadronic EOSs in the vicinity of $n_s = 0.16 \text{ fm}^{-3}$. The range of pressures at n_s is approximately a factor of six. This figure is taken from and the EOS names are identified in Reference 13.

cases are not shown in **Figure 3**). However, in contrast to the expectation that $R \propto K^{1/2}$ when $\gamma \sim 2$, it has been shown phenomenologically (13) that the scaling is approximately $R \propto p_s^{1/4}$; the reduced exponent is due to general relativistic effects. Note that the ordering of radii for 1.4-$M_\odot$ neutron stars in **Figure 3** is commensurate with the ordering of p_s values in **Figure 2**.

In contrast, at low central densities where the pressure is dominated by degenerate relativistic electrons and $\gamma \sim 4/3$, we should expect M at a given R to scale as $M \propto K^{3/2}$. Indeed, two families of hadronic stars are evident (EOSs AP4, ENG, AP3, and MPA1 constitute one family in **Figure 3**) due to each family's relative values of p_s (**Figure 2**). Thus, M for a given R on the horizontal part and R for a given M on the vertical part increase with p_s.

The pressure in the vicinity of n_s for neutron star matter is an important property of the nuclear EOS. It is traditional to express the energy per baryon of hadronic matter near n_s as a double Taylor expansion in $n - n_s$ and neutron excess $1 - 2x$, where x is the proton fraction:

$$e(u, x) = -B + \frac{K_o}{18}(u - 1)^2 + \frac{K_o'}{162}(u - 1)^3 + S_2(u)(1 - 2x)^2 + e_\ell + \cdots. \qquad 4.$$

Here, $B \simeq 16$ MeV is the bulk binding energy of symmetric matter at n_s; K_o and K_o' are the standard incompressibility and skewness parameters, respectively; $S_2(u)$ is the symmetry energy to quadratic order in $1 - 2x$; e_ℓ is the lepton energy; and $u = n/n_s$. For bulk matter in β equilibrium, when $u \gtrsim 0.01$ and $x \ll 1$, the leptonic contributions are small. If higher-order rather than quadratic terms in the neutron excess are unimportant, then $S_2(u) \simeq S(u)$, where $S(u)$, the total symmetry energy, is the difference between pure neutron ($x = 0$) and symmetric ($x = 1/2$) matter
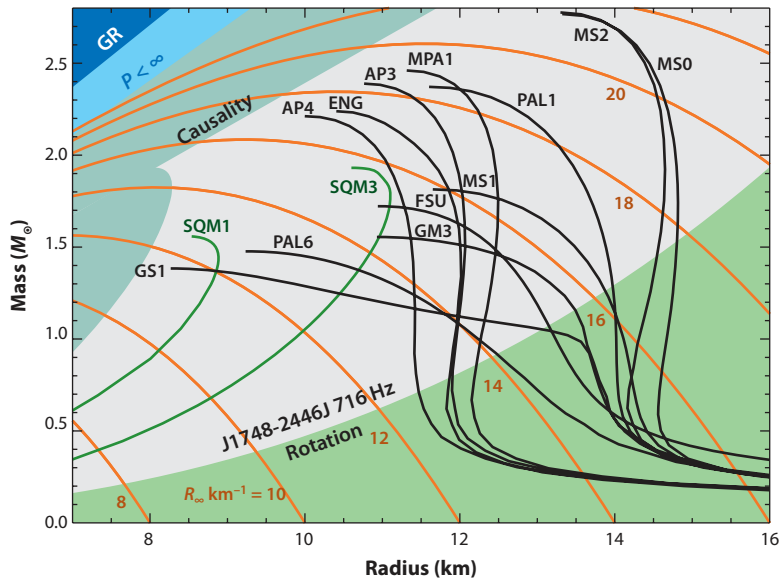
Figure 3

Typical $M-R$ curves for hadronic equations of state (EOSs) (*black curves*) and strange quark matter (SQM) EOSs (*green curves*). The EOS names are given in Reference 13, and their $P-n$ relations are displayed in **Figure 2**. Regions of the $M-R$ plane excluded by general relativity (GR), finite pressure, and causality are indicated. The orange curves show contours of $R_\infty = R(1 - 2\,GM/Rc^2)^{-1/2}$. The region marked rotation is bounded by the realistic mass-shedding limit for the highest-known pulsar frequency, 716 Hz, for PSR J1748-2446J (14). Figure adapted from Reference 15.

energies. The pressure is

$$p(u, x) = u^2 n_s \left(\frac{\partial e}{\partial u}\right)_x \simeq u^2 n_s \left[\frac{K_o}{9}(u - 1) + \frac{K_o'}{54}(u - 1)^2 + \frac{dS_2}{du}(1 - 2x)^2\right] + p_\ell + \cdots, \quad 5.$$

where p_ℓ is the lepton pressure. In the vicinity of $u \simeq 1$, with $x \ll 1$, p_ℓ is small and the pressure is almost completely determined by dS_2/du. Laboratory constraints on the nuclear symmetry energy are discussed in Section 6.

2.2. The Maximally Compact Equation of State

Koranda et al. (16) suggested that absolute limits to neutron star structure could be found by considering a soft low-density EOS coupled with a stiff high-density EOS, which would maximize the compactness M/R. The limiting case of a soft EOS is $p = 0$. The limiting case of a stiff EOS is $dp/d\varepsilon = (c_s/c)^2 = 1$, where c_s is the adiabatic speed of sound that should not exceed the speed of light; otherwise, causality would be violated. The maximally compact EOS is therefore defined by

$$p = 0 \quad \text{for } \varepsilon < \varepsilon_0; \qquad p = \varepsilon - \varepsilon_0 \quad \text{for } \varepsilon > \varepsilon_0. \qquad 6.$$

This EOS has a single parameter, ε_0, and therefore the structure equations (Equation 2) can be expressed in a scale-free way:

$$\frac{dw}{dx} = -\frac{(y + 4\pi x^3 w)(2w - 1)}{x(x - 2y)}; \quad \frac{dy}{dx} = 4\pi x^2 w. \qquad 7.$$

Here, $w = \varepsilon/\varepsilon_0$, $x = r\sqrt{G\varepsilon_0}/c^2$, and $y = m\sqrt{G^3\varepsilon_0}/c^4$. Varying the value of w at the origin (w_0) gives rise to a family of solutions described by dimensionless radius X and total mass Y. The

maximally compact solution has the largest value of Y, which occurs when $w_0 = 3.034$, $X_c = 0.2404$, and $Y_c = 0.08513$. Because $X_c/Y_c = 2.824$ for this case, stable configurations satisfy

$$R \geq 2.824 \frac{GM}{c^2}, \quad z = \left(1 - \frac{2GM}{Rc^2}\right)^{-1/2} - 1 \leq 0.8512, \qquad 8.$$

where z is the redshift. This limiting redshift is close to the result obtained by Lindblom (17). It is also clear that the neutron star maximum mass is

$$M_{max} = Y_c \frac{c^4}{\sqrt{G^3 \varepsilon_0}} \simeq 4.09 \sqrt{\frac{\varepsilon_s}{\varepsilon_0}} M_\odot. \qquad 9.$$

This result is similar to that found by Rhoades & Ruffini (18): If the low-density EOS is known up to $\approx 2\varepsilon_s$, causality limits the neutron star maximum mass to approximately $3\,M_\odot$.

The maximally compact solution also implies that

$$\varepsilon_c \leq 0.02199\, \varepsilon_0 Y_c^{-2} \simeq 50.8\, \varepsilon_s (M_\odot/M_{max})^2. \qquad 10.$$

This relation (**Figure 4**) states that the largest measured neutron star mass, given that it is lower than the true neutron star maximum mass, must set an upper limit on the central density of any neutron star (19) and, by extension, that it must also limit the central pressure to values lower than $34.0\varepsilon_s (M_\odot/M_{max})^2$.

The scale-free character of the maximally compact solution can be extended to axial symmetry in general relativity with no additional parameters (16), and the minimum spin period, limited by
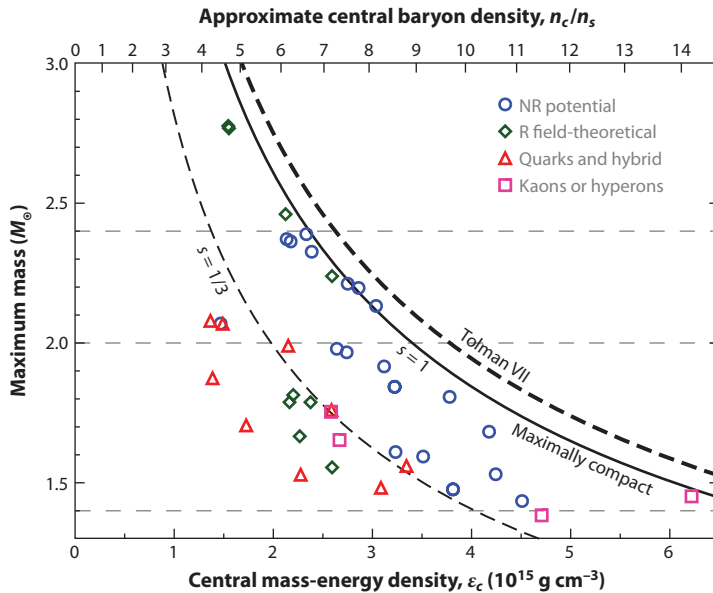

Figure 4

The relation between the maximum mass and the central density predicted by the maximally compact equation of state (EOS) (Equation 10) is shown by the curve $s = 1$. Results for different classes of EOSs are indicated: nonrelativistic (NR) potential or Skyrme-like EOSs (*open circles*), relativistic (R) field-theoretical EOSs (*diamonds*), EOSs containing significant amounts of quarks (*triangles*), and EOSs with significant meson condensates or hyperons (*squares*). The $M_{max} - \varepsilon_c$ relations predicted by causality coupled with the Tolman VII solution (20) and the EOS $p = (\varepsilon - \varepsilon_0)/3$ are also indicated. The latter effectively bounds stars containing quarks. Adapted from Reference 19.

mass shedding at the equator, occurs for the maximum mass configuration and scales with $1/\sqrt{\varepsilon_0}$. The result can be expressed as

$$P_{\min} = 0.74 \left(\frac{M_\odot}{M_{\max}} \right)^{1/2} \left(\frac{R_{\max}}{10\,\text{km}} \right)^{3/2} \text{ms} = 0.20 \left(\frac{M_{\max}}{M_\odot} \right) \text{ms},$$

11.

where $M_{\max}$ and $R_{\max}$ correspond to values for the nonrotating star. This equation represents the formal limit imposed by causality on the spin period, but a more realistic limit for an arbitrary neutron star with nonrotating values M and R, which has been phenomenologically determined (21), replaces the coefficient 0.74 ms in Equation 11 with 0.96 ms, and $M_{\max}$ and $R_{\max}$ with M and R (**Figure 3**). Also, Lattimer & Prakash (22) have shown that the maximum fractional binding energy and the baryon chemical potential are 25.2% and $\mu_{B,\max} = 2.093$ GeV, respectively, independent of ε_c and $M_{\max}$.

The MIT bag model EOS can be expressed as $p = (\varepsilon - \varepsilon_0)/3$, where $\varepsilon_0 = 4B$, so the sound speed is $c_s = c/\sqrt{3}$ everywhere. The solution of Equation 2 with this EOS may also be expressed in a scale-free manner, with maximum mass eigenvalues $w_0 = 4.826$, $X_c = 0.1910$, $Y_c = 0.05169$, and $X_c/Y_c = 3.696$. Thus, the $M_{\max} - \varepsilon_c$ relation mirrors that of Equation 10 but is a factor of $0.05169/0.08513 = 0.607$ lower (**Figure 4**). Interestingly, this curve apparently bounds the central densities of not only pure SQM stars but also stars containing significant amounts of quarks in a pure or mixed state with hadrons, even though the quark matter EOSs that are used can be more complex than the MIT bag model. This observation has important consequences for the quark-hadron phase transition density if deconfined quarks appear in neutron stars, as we discuss further below.

Obviously, the largest precisely known neutron star mass sets a lower bound to $M_{\max}$. A lower bound to $M_{\max}$ also further restricts the allowed $M-R$ region beyond the area excluded by causality, $R \leq 2.824\, GM/c^2$ (**Figure 3**). Conversely, the precise measurements of any neutron star's mass and radius establish an upper bound to $M_{\max}$. **Figure 5** depicts these model-independent features and shows $M-R$ contours for the maximally compact EOS with various values of ε_0. Each contour
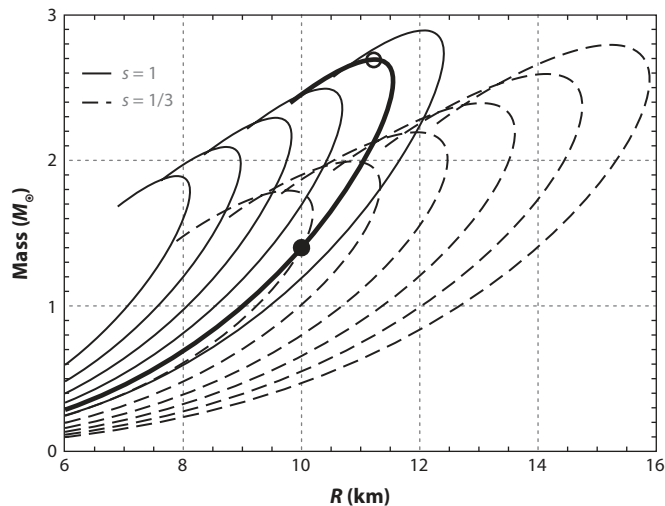

Figure 5

Mass-radius contours with various values of $M_{\max}$ for the maximally compact equation of state (EOS) $p = \varepsilon - \varepsilon_0$ are shown as solid lines. Contours for the EOS $p = (\varepsilon - \varepsilon_0)/3$ are shown as dashed lines. A precise (M, R) measurement (*filled circle*) sets an upper limit on $M_{\max}$ (*open circle*) (2.69 $M_\odot$).

represents the minimum radius possible for a given mass, given the contour's value of M_{max}. For example, if $M_{max} \gtrsim 2\,M_\odot$, a 1.4-$M_\odot$ neutron or quark star necessarily has $R \gtrsim 8.25$ km. It also follows that any M−R curve passing through a given (M, R) point has a smaller value of M_{max} than that of the maximally compact EOS passing through the same (M, R) point. This hypothesis can be easily demonstrated by overlaying M−R trajectories for an alternate EOS, such as the MIT bag-like model, $p = (\varepsilon - \varepsilon_0)/3$ (**Figure 3**). For the indicated point (1.4 $M_\odot$, 10 km), this alternate EOS has a maximum mass of only 1.79 $M_\odot$, whereas the maximum mass of the maximally compact EOS is 2.69 $M_\odot$.

3. NEUTRON STAR MASSES

3.1. Mass Measurements

The most accurate measurements concerning neutron stars are mass determinations from pulsar timing. To date, approximately 33 relatively precise masses have become available. In these systems, five Keplerian parameters can be precisely measured (23); these parameters include the binary period P, the projection of the pulsar's semimajor axis on the line of sight $a_p \sin i$ (where i is the orbit's inclination angle), the eccentricity e, and the time T_0 and longitude ω of periastron. Two of these observables yield a mass function,

$$f_p = \left(\frac{2\pi}{P}\right)^2 \frac{(a_p \sin i)^3}{G} = \frac{(M_c \sin i)^3}{M^2}, \qquad 12.$$

where $M = M_p + M_c$ is the total mass, M_p is the pulsar mass, and M_c is the companion mass. The minimum possible companion mass M_c is equal to f_p.

The inclination angle i is often the most difficult parameter to infer, but even if it were known a priori, the above equation would specify a relation between only M_p and M_c, unless the mass function f_c of the companion were also measurable. The mass function of the companion is measurable in the rare case when the companion itself is a detectable pulsar or a star with an observable spectrum, as in an X-ray binary. Fortunately, binary pulsars are compact systems, and general relativistic effects can often be observed. These effects include the advance of the periastron of the orbit,

$$\dot{\omega} = 3 \left(\frac{2\pi}{P}\right)^{5/3} \left(\frac{GM}{c^3}\right)^{2/3} (1 - e^2)^{-1}; \qquad 13.$$

the combined effect of variations in the transverse Doppler shift and gravitational redshift (time dilation) around an elliptical orbit,

$$\gamma = e \left(\frac{P}{2\pi}\right)^{1/3} \frac{M_c(M + M_c)}{M^{4/3}} \left(\frac{G}{c^3}\right)^{2/3}; \qquad 14.$$

the orbital period decay due to the emission of gravitational radiation,

$$\dot{P} = -\frac{192\pi}{5} \left(\frac{2\pi G}{c^3}\right)^{5/3} \left(1 + \frac{73}{24}e^2 + \frac{37}{96}e^4\right)(1 - e^2)^{-7/2} \frac{M_p M_c}{M^{1/3}}; \qquad 15.$$

and the Shapiro time delay (24), caused by the propagation of the pulsar signal through the gravitational field of its companion. The relativistic Shapiro delay produces a delay in pulse arrival time (25),

$$\delta_S(\phi) = 2 \frac{GM_c}{c^3} \ln \left[\frac{1 + e \cos \phi}{1 - \sin(\omega + \phi)\sin i}\right], \qquad 16.$$
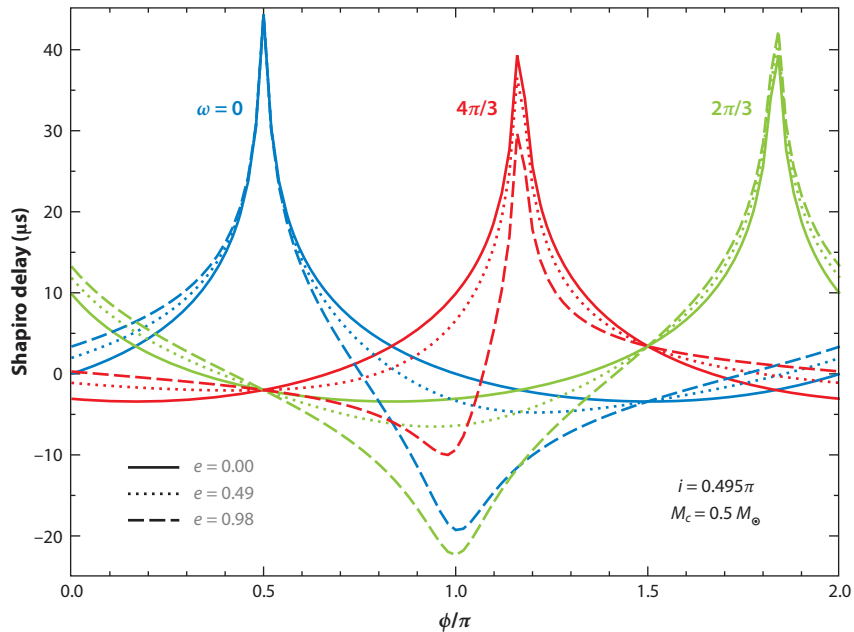
Figure 6

Shapiro delay for various values of eccentricity e and periastron longitude ω, assuming an orbital inclination of $i = 0.495\pi$ radians.

where ϕ is the true anomaly, the angular parameter defining the position of the pulsar in its orbit relative to the periastron. δ_S is a periodic function of ϕ with an amplitude

$$\Delta_S = 2 \frac{GM_c}{c^3} \left| \ln \left[\left(\frac{1 + e \sin \omega}{1 - e} \right) \left(\frac{1 + \sin \omega \sin i}{1 - \sin i} \right) \right] \right|, \qquad 17.$$

which is very large for extremely eccentric ($e \sim 1$) and/or nearly edge-on ($\sin i \sim 1$) binaries. For a circular orbit with $i \simeq \pi/2$,

$$\Delta_S \simeq 4 \frac{GM_c}{c^3} \ln \left(\frac{2}{\cos i} \right). \qquad 18.$$

The scale of the Shapiro delay is set by the constant $GM_\odot/c^2 = 4.9255$ µs, and both the amplitude and the shape of the Shapiro delay constrain i, ω, and e (**Figure 6**).

The inclination angle, and the individual masses, can be constrained by measurements of two or more of these effects, which is possible only in extremely compact systems. Observation of a single relativistic effect is not sufficient to constrain both masses. Only a small fraction of pulsars in binaries have two or more well-measured relativistic effects that enable precise measurements of the pulsar mass. In some cases (**Table 1**), an empirical relation (26) between the binary period and the WD companion mass proves useful. In cases in which the companion is optically detected, spectral observations can provide the WD mass and the radial velocity amplitude, which can be used to establish the system's mass ratio. In some cases (e.g., References 27 and 28), the inclination angle can be restricted by the detection of changes in the projected semimajor axis $x = a_p \sin i$ caused by the system's proper motion (29),

$$\tan i = \frac{x \mu \sin \theta}{dx/dt}, \qquad 19.$$

Table 1 Neutron star mass measurements, 1-σ uncertainties, $M > 0.9\,M_\odot$ assumed

Object	Mass ($M_\odot$)	Reference	Object	Mass ($M_\odot$)	Reference
X-ray/optical binaries (mean, 1.568 $M_\odot$; error-weighted mean, 1.368$M_\odot$)					
4U 1700-377[a]	$2.44^{+0.27}_{-0.27}$	32	Vela X-1	$1.770^{+0.083}_{-0.083}$	33
Cyg X-2	$1.71^{+0.21}_{-0.21}$	34	4U 1538-52	$1.00^{+0.10}_{-0.10}$	33
SMC X-1	$1.037^{+0.085}_{-0.085}$	33	LMC X-4	$1.285^{+0.051}_{-0.051}$	33
Cen X-3	$1.486^{+0.082}_{-0.082}$	33	Her X-1	$1.073^{+0.358}_{-0.173}$	33
XTE J2123-058	$1.53^{+0.30}_{-0.42}$	35; J. Tomsick, private communication	2S 0921-630	$1.4^{+0.1}_{-0.1}$	36
4U 1822-371	$1.96^{+0.36}_{-0.35}$	37	EXO 1722-363	$1.545^{+0.465}_{-0.465}$	38
B1957+20	$2.39^{+0.36}_{-0.29}$	39	IGR J18027-2016	$1.47^{+0.38}_{-0.32}$	40
OAO 1657-415	$1.42^{+0.26}_{-0.26}$	41	—	—	—
Neutron star–neutron star binaries (mean, 1.322 $M_\odot$; error-weighted mean, 1.402 $M_\odot$)					
J1829+2456[b]	$1.25^{+0.11}_{-0.35}$	42	Companion	$1.34^{+0.37}_{-0.10}$	42
J1811-1736[b]	$1.53^{+0.22}_{-0.63}$	43	Companion	$1.04^{+0.73}_{-0.12}$	43
J1906+0746	$1.248^{+0.018}_{-0.018}$	44	Companion	$1.365^{+0.018}_{-0.018}$	44
J1518+4904	$1.23^{+0.00}_{-0.33}$	27	Companion	$1.49^{+0.33}_{-0.00}$	27
B1534+12	$1.3332^{+0.0010}_{-0.0010}$	45	Companion	$1.3452^{+0.0010}_{-0.0010}$	45
B1913+16	$1.4398^{+0.0002}_{-0.0002}$	46	Companion	$1.3886^{+0.0002}_{-0.0002}$	46
B2127+11C[d]	$1.358^{+0.010}_{-0.010}$	47	Companion	$1.354^{+0.010}_{-0.010}$	47
J0737-3039A	$1.3381^{+0.0007}_{-0.0007}$	48	J0737-3039B	$1.2489^{+0.0007}_{-0.0007}$	48
J1756-2251	$1.312^{+0.017}_{-0.017}$	49	Companion	$1.258^{+0.017}_{-0.017}$	49
J1807-2500B[d]	$1.3655^{+0.0020}_{-0.0020}$	30	Companion?	$1.2064^{+0.0020}_{-0.0020}$	30
Neutron star–white dwarf binaries (mean, 1.543 $M_\odot$; error-weighted mean, 1.369 $M_\odot$)					
B2303+46	$1.38^{+0.06}_{-0.10}$	31	J1012+5307	$1.64^{+0.22}_{-0.22}$	50
J1713+0747[b]	$1.53^{+0.08}_{-0.06}$	51	B1802-07[d]	$1.26^{+0.08}_{-0.17}$	31
B1855+09[b]	$1.57^{+0.12}_{-0.11}$	52	J0621+1002	$1.70^{+0.10}_{-0.17}$	53
J0751+1807	$1.26^{+0.14}_{-0.14}$	53	J0437-4715	$1.76^{+0.20}_{-0.20}$	54
J1141-6545	$1.27^{+0.01}_{-0.01}$	55	J1748-2446I[d]	$1.91^{+0.02}_{-0.10}$	56
J1748-2446J[d]	$1.79^{+0.02}_{-0.10}$	56	J1909-3744[d]	$1.47^{+0.03}_{-0.02}$	57
J0024-7204H[d]	$1.48^{+0.03}_{-0.06}$	56	B1802-2124	$1.24^{+0.11}_{-0.11}$	58
J0514-4002A[d]	$1.49^{+0.04}_{-0.27}$	56	B1516+02B[d]	$2.08^{+0.19}_{-0.19}$	59
J1748-2021B[d]	$2.74^{+0.21}_{-0.21}$	60	J1750-37A[d]	$1.26^{+0.39}_{-0.36}$	60
J1738+0333	$1.55^{+0.55}_{-0.55}$	62	B1911-5958A[d]	$1.34^{+0.08}_{-0.08}$	63
J1614-2230	$1.97^{+0.04}_{-0.04}$	64	J2043+1711[c]	$1.85^{+0.15}_{-0.15}$	65
J1910+1256[c]	$1.6^{+0.6}_{-0.6}$	28	J2106+1948[c]	$1.0^{+0.5}_{-0.1}$	28
J1853+1303[c]	$1.4^{+0.7}_{-0.5}$	28	J1045-4509	$1.19^{+0.29}_{-0.29}$	31
J1804-2718	$1.3^{+0.4}_{-0.4}$	31	J2019+2425	$1.205^{+0.305}_{-0.305}$	66
Neutron star–main sequence binaries					
J0045-7319	$1.58^{+0.34}_{-0.34}$	31	J1903+0327[e]	$1.667^{+0.021}_{-0.021}$	67

[a]Black hole due to lack of pulsations?

[b]Companion masses are from Reference 31.

[c]Binary period–white dwarf masses are from Reference 26.

[d]Globular cluster binary.

[e]3-σ error.

where θ is the unknown angle between the directions of the proper motion and the ascending node of the pulsar's orbit. Use of $\sin\theta < 1$ results in an upper limit to i if μ, dx/dt, and x are measured, assuming it is known that dx/dt is not due to gravitational radiation or perturbations caused by a third component.

In eclipsing X-ray binaries containing pulsars, the combination of radio timing data and X-ray observations yields the orbital period, the eccentricity, the longitude of periastron, the pulsar's orbital semimajor axis, and the eclipse duration. Optical data can also provide the radial velocity amplitude of the companion and geometric information about the companion's shape. WD masses or surface gravities can be estimated from spectral measurements and effective temperatures, if the distances are known. Less accurate measurements of neutron star masses can be achieved for X-ray binaries, in which X-rays are emitted by matter accreting onto a neutron star from a companion star that is filling its Roche lobe. Both X-ray and optical observations can yield both mass functions, f_p and f_c, but f_c can be subject to large uncertainties due to the faintness of optical radiation. In some cases, the neutron star is a pulsar that establishes f_p. Limits to inclination can also be set according to the presence or absence of eclipses, given that companions in X-ray binaries are not compact objects.

Figure 7 and **Table 1** summarize the available mass information from pulsars in binaries. These summaries represent an update of those found in Reference 22; I maintain a contemporary table, figure, and references at **http://www.stellarcollapse.org**. Cases in which the standard millisecond pulsar-formation model (26) has been used to constrain the neutron star mass are explicitly indicated in **Table 1**. Also, it has not yet been confirmed that the companion of PSR J1807-2500B (30) is a neutron star. This system has the highest companion mass of any recycled pulsar.

3.2. The Neutron Star Maximum Mass

From the perspective of EOS constraints, the most massive neutron stars are key. There is now ample observational support from pulsars for neutron stars with masses significantly greater than $1.5\,M_\odot$. These include PSR J1903+0327 (67), which has a main-sequence companion; the globular cluster pulsars PSR 1748-2446 I and PSR 1748-2446 J (56), PSR J1748-2021B (59), PSR B1516+02B (60), PSR J2043+1711 (65), and PSR J1614-2230 (64), all of which have WD companions; and the black widow pulsar PSR B1957+20 (39). The inclination angles of the two binaries containing pulsars I and J in the globular cluster Ter 5 are unconstrained by observation, but if their inclinations are random, there is a 95% chance that at least one of these pulsars is greater than $1.68\,M_\odot$ (68). The WD binary period–mass relation (26) was used to restrict the inclination of PSR J2043+1711. Inclinations are unknown for PSR J1748-2021B and PSR B1516+02B and are assumed to be random, but this assumption is dangerous because the systems are not randomly selected.

The largest well-measured mass is $1.97 \pm 0.04\,M_\odot$ for PSR J1614-2230 (64), for which i has been determined by detection of the Shapiro time delay. This 3.15-ms pulsar has an 8.7-day, nearly circular orbit with a 0.5-$M_\odot$ companion. For this binary, $a_p \sin i = 11.3$ light seconds and $\sin i = 0.99989$; in other words, it is virtually edge-on. The Shapiro time delay amplitude (from Equation 18), is 48.8 μs. By virtue of its accuracy, this mass has become the standard for the minimum value of the neutron star maximum mass.

In addition, a few X-ray binaries seem to contain high-mass neutron stars: approximately $1.8\,M_\odot$ in the case of Vela X-1 (33), $2\,M_\odot$ for 4U 1822-371 (37), and $2.4\,M_\odot$ for 4U 1700-377 and PSR B1957+20 (39). Nonetheless, the large systematic errors inherent in X-ray binary mass measurements warrant caution.
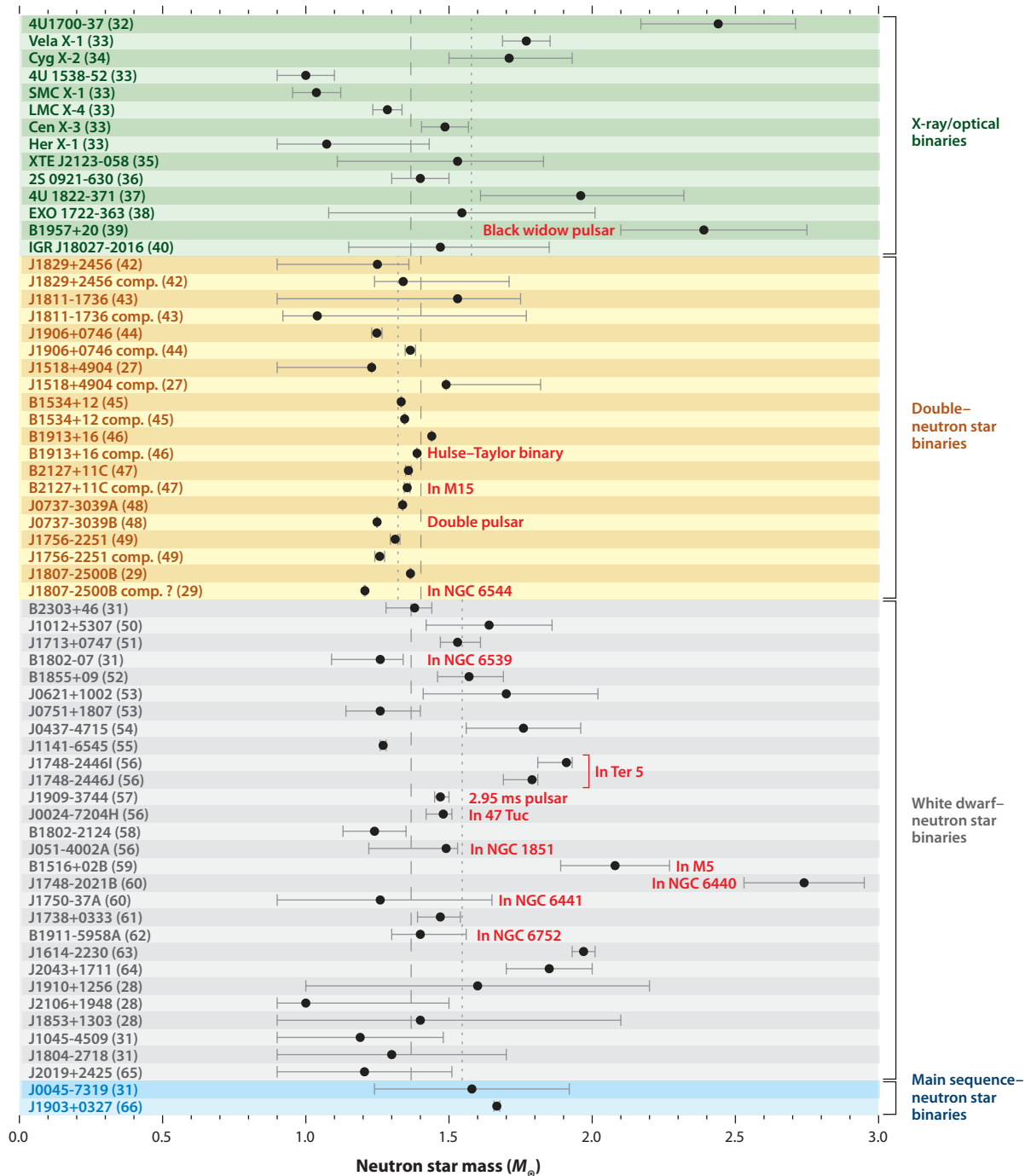
Figure 7

Measured neutron star masses with 1-σ errors. References in parentheses following source names are identified in **Table 1**.

The case of the black widow pulsar, PSR B1957+20, represents an intriguing case. This system has both pulsar timing and optical light-curve information that yield both a mass function and an estimate of the inclination i from the shape of the light curve (69). The binary consists of a 1.6-ms pulsar in a 9.17-h, nearly circular orbit around an extremely low mass companion: $M_c \simeq 0.03\, M_\odot$. The pulsar is eclipsed for approximately 10% of each orbit, but considering that $a_p \sin i = 0.089$ light seconds $= 0.038\, R_\odot$ and that $a_c \sin i \sim 3\, R_\odot$ is $M_p/M_c \simeq 80$ times larger, the eclipsing object has to be approximately $0.1 a_c \sin i \sim 0.3\, R_\odot$—much larger than the size of the companion star. Irradiation of the companion by the pulsar strongly heats its near side to the point of ablation, which leads to a comet-like tail and a large cloud of plasma that is believed to be responsible for the eclipses. The pulsar is literally consuming its companion, hence the name black widow; it has reduced its companion's mass to a small fraction of its original mass. (In fact, several black widow systems are known.) The irradiation also produces an enormous (factor-of-100) variation in the brightness of the companion during its orbit. The companion is bloated and nearly fills its Roche lobe. The companion's optical light curve allows one to estimate the mass ratio M_p/M_c and the inclination angle i. However, the large size of the companion means that the "center of light" of the system is not equivalent to its center of mass: The optical light curve depends on the projected semimajor axis of the irradiated near side of the companion, rather than the projected semimajor axis of the center of mass of the companion. The extreme case is either that the companion has zero radius or that it completely fills its Roche lobe, leading to a range $1.7 < M_p/M_\odot < 3.2$, but estimates based on modeling have reduced the probable range to $2.4 \pm 0.4\, M_\odot$. It will be valuable to extend observations and modeling of this system because a 2.4-$M_\odot$ neutron star would have profound implications.

3.3. The Minimum Neutron Star Mass

In addition to large measured masses, there is increasing evidence for small neutron stars. Three X-ray binaries (33) and two neutron stars in double–neutron star binaries have best estimates of less than approximately $1.1\, M_\odot$, although in all cases the error bars are substantial. The most interesting low-mass candidates are SMC X-1 and 4U 1538-52, which have 1-σ upper limits to mass of $1.122\, M_\odot$ and $1.10\, M_\odot$, respectively. Özel et al. (70) reanalyzed these systems without the effects of the ellipsoidal shapes of the companion stars on the optical light curves and found masses of $0.93 \pm 0.12\, M_\odot$ and $1.18 \pm 0.25\, M_\odot$, respectively. According to either analysis, at least one of these systems has a very low neutron star mass.

Neutron star masses lower than $1.2\, M_\odot$ would challenge the paradigm of gravitational-collapse neutron star formation. The iron cores of 8–10-$M_\odot$ progenitor stars are approximately the Chandrasekhar baryon mass, which, corrected for electron fractions Y_e of less than 0.5 and for finite temperatures, are approximately $1.25\, M_\odot$. The lowest-mass neutron stars may form from such progenitor stars in so-called electron-capture supernovae, in which an oxygen-neon-magnesium (O-Ne-Mg) core collapses as pressure support is lost due to electron captures on Ne and/or Mg nuclei (71). Electron captures are triggered by density increases due to accretion in binaries. Correcting for binding, the lowest-gravitational-mass neutron star could be 1.15–$1.2\, M_\odot$.

A low-mass limit is also suggested by thermodynamics. All gravitational-collapse supernova models, including O-Ne-Mg accretion-induced collapses, produce hot, lepton-rich proto–neutron stars due to neutrino trapping during infall. Lepton fractions $Y_\ell = Y_e + Y_\nu$ (where Y_ν is the net number of electron neutrinos per baryon) of order 0.3–0.35, and entropies per baryon $s \sim 1$, exist in the centers of neutron stars at birth, according to current simulations. Within 10 s, Y_ν within the star drops to zero through diffusion, but the bulk of the neutrino energy remains in the remnant as thermal energy (72). Compared with cold, catalyzed stars in β equilibrium without neutrinos ($Y_\nu = 0$), which have a minimum mass of order $0.09\, M_\odot$ (as discussed in Section 2.1),

proto–neutron stars have a minimum gravitational mass of order 0.9–1.2 $M_\odot$, depending on the entropy profile within the star (73). Masses at the higher end of this range are suggested for configurations with strongly shocked outer cores. Masses smaller than the minimum are dynamically unstable and cannot lead to stable neutron stars.

In summary, the current gravitational-collapse paradigm for cores of massive stars that lead to hot, lepton-rich proto–neutron stars and successful supernova explosions imposes a lower limit on neutron star masses at birth. Neutron star masses can increase due to fallback after the explosion and accretion from binary companions, but they cannot further decrease except during a catastrophic merger. Given the observational errors, the lowest observed masses are not currently incompatible with this paradigm, but this remains an interesting problem.

3.4. The Distribution of Neutron Star Masses

Most neutron stars have masses close to 1.3 to 1.4 $M_\odot$, but lower and higher masses exist. Evolution probably plays many roles in the distribution of neutron star masses: To name only two considerations, the neutron star birth mass seems to depend on progenitor mass, and accretion can lead to the accumulation of several tenths of a solar mass over a star's life. The observed masses (**Table 1**) may be separated into four groups that could have different evolutionary histories: X-ray binaries, double–neutron star binaries, WD–neutron star binaries, and WD–neutron star binaries found in globular clusters. **Figure 8** shows histograms of masses for these four groups,
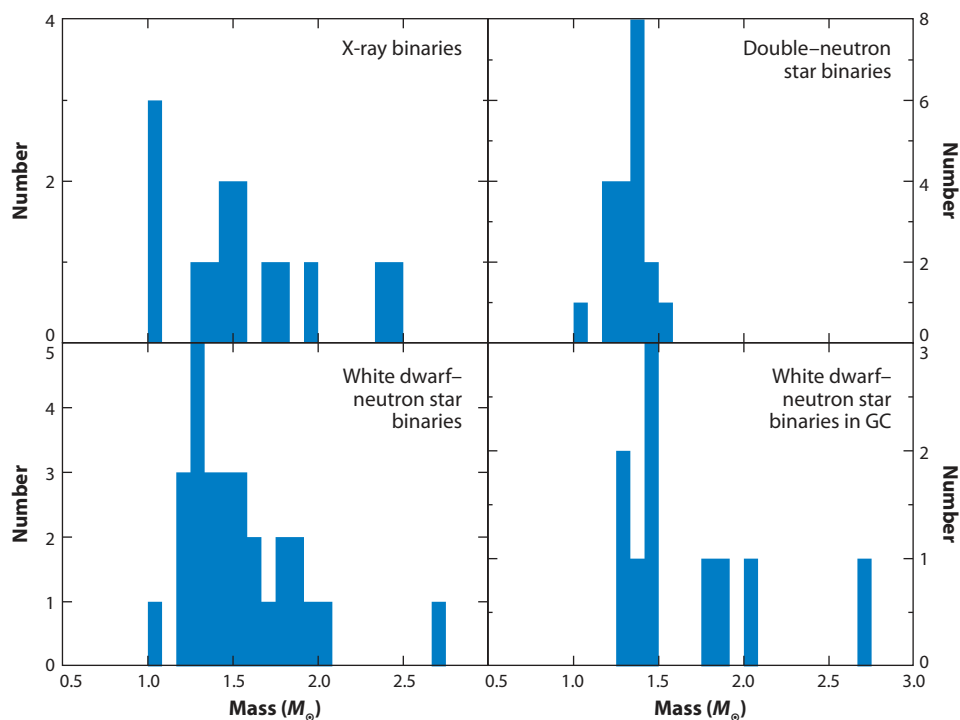
Figure 8

Histograms of neutron star masses for four groups: X-ray binaries, double–neutron star binaries, white dwarf–pulsar binaries, and white dwarf–pulsar binaries in globular clusters (GCs). Bins are taken to be 0.08333 $M_\odot$ in width.
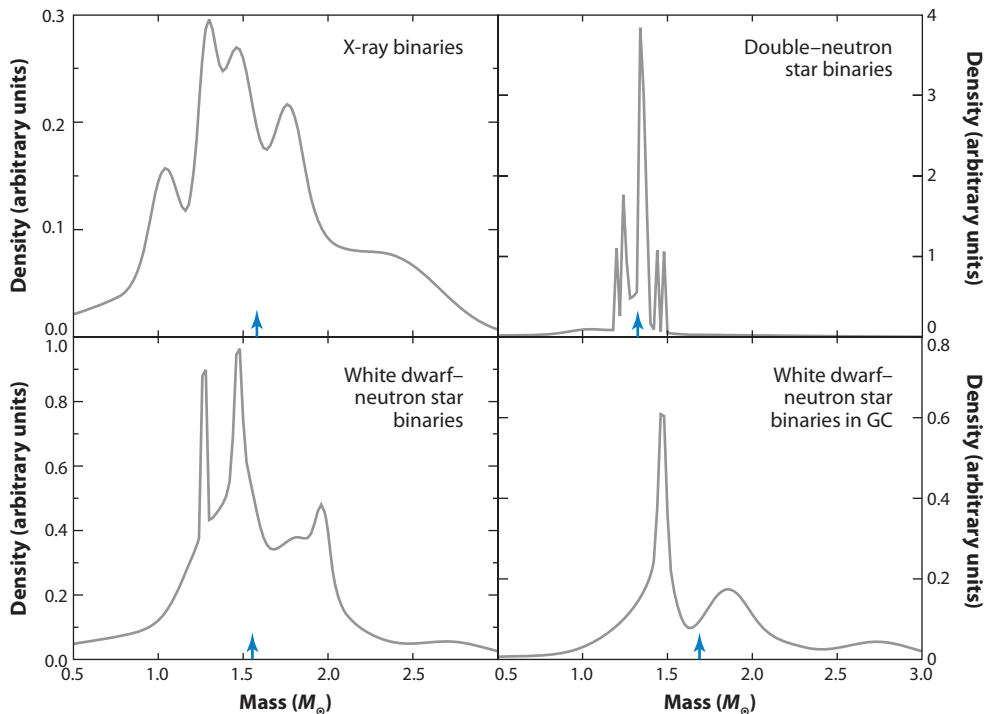
Figure 9

The density of neutron star masses, namely the number of stars per mass interval, is shown for the four groups of neutron stars displayed in **Figure 8**. The weighted average mass is indicated by the arrow in each plot.

but they are of limited utility given that individual stars can have significant mass errors (1-σ errors are provided in **Table 1**). Interestingly, the first three groups in **Table 1** have the same error-weighted average masses to within 0.03 $M_\odot$.

To account for errors, one can approximate each star with a Gaussian probability distribution whose integral over mass is unity. The histograms are thereby transformed into a plot of the number of stars in a small mass interval, or a density, as a function of mass. Those stars with large errors have a relatively small contribution at any mass; those with small errors contribute only over a very narrow range of masses. **Figure 9** shows these densities.

The most significant feature of the distribution of X-ray binaries is a broad maximum. However, the distribution of double neutron stars is very narrow and peaks at 1.33 $M_\odot$. The distribution of WD–neutron star binaries is more complex; there is evidence for three groups with peaks at 1.25 $M_\odot$, 1.45 $M_\odot$, and ~1.9 $M_\odot$. The last two peaks are also prominent in the distribution of pulsar masses with WD companions in globular clusters. Zhang et al. (74) noted the existence of the first two groups. They identified the first group with periods greater than 20 ms as nonrecycled pulsars and the second group with smaller periods as recycled pulsars that have experienced extended mass-accretion episodes. An analysis by Özel et al. (70) concluded that there are three groups: the first with a mean of 1.28 $M_\odot$ and a dispersion of 0.24 $M_\odot$ in nonrecycled high-mass binaries; the second (representing stars in double–neutron star systems) with a mean of 1.33 $M_\odot$ and a dispersion of 0.06 $M_\odot$; and a third containing recycled pulsars with a mean of 1.48 $M_\odot$.

However, Schwab et al. (75) argued for two peaks at low masses: 1.25 $M_\odot$ and 1.35 $M_\odot$. The first peak represents neutron star production via O-Ne-Mg supernovae, and the second

peak represents neutron star production through conventional iron core collapse. The existence of two types of supernovae—iron core-collapse supernovae from high-mass progenitors and electron-capture supernovae from low-mass O-Ne-Mg cores—is supported by statistics of neutron star–hosting X-ray binaries. Knigge et al. (76) show that these binaries are composed of two subpopulations differentiated by spin periods, orbital periods, and orbital eccentricities. Those with short spin and orbital periods and low eccentricities probably originate from O-Ne-Mg accretion–induced collapses.

The study by Podsiadlowski et al. (77) demonstrates that the pulsar and companion stars in double–neutron star binaries appear to be drawn from the same distribution. Their small dispersions could be attributed to their birth in O-Ne-Mg supernovae, whose helium (He) cores are expected to have a small mass range (1.36–1.38 $M_\odot$) prior to collapse. Özel et al.'s study also indicates that although the mean mass of the lowest group of WD–neutron star binaries is nearly the same as that of the double–neutron star binaries, the dispersion of the former appears greater. How significant this finding is, however, depends on the details of fitting the optical light curves in these systems.

In contrast, Kiziltan et al. (56) claimed that there is significant evidence for only two groups centered at 1.35 $M_\odot$ and 1.5 $M_\odot$. Presumably only the higher-mass group has experienced considerable accretion.

4. SIMULTANEOUS MASS AND RADIUS MEASUREMENTS

In contrast to mass determinations, there are no high-accuracy radius measurements. Moreover, there are no radius measurements for any neutron star with a precise mass determination. Many astrophysical observations that could lead to the extraction of neutron star radii, or combined mass and radius constraints, have been proposed. These observations include the following.

1. Thermal X-ray and optical fluxes from isolated and quiescent neutron stars (78).
2. Type I X-ray bursts on neutron star surfaces (79).
3. Quasi-periodic oscillations from accreting neutron stars (80).
4. Spin-orbit coupling, observable through pulsar timing in extremely compact binaries, leading to moments of inertia (81).
5. Pulsar glitches, which constrain properties of neutron star crusts (82).
6. Cooling following accretion episodes in quiescent neutron stars that also constrain crusts (83).
7. Neutron star seismology from X-rays observed from flares from soft γ-ray repeaters (84).
8. Pulse profiles in X-ray pulsars, which constrain M/R ratios due to gravitational light bending (85).
9. Gravitational radiation from tidal disruption of merging neutron stars (7).
10. Neutrino signals from proto–neutron stars formed in Galactic supernovae (72).

Of these proposed observations, thermal emission and X-ray bursts from neutron star surfaces have dominated recent attempts to infer neutron star radii.

4.1. Thermal Emission from Quiescent and Isolated Sources

Until a million years after a star's birth, neutrino emission dominates thermal emission from the surface, but the star is observable as an X-ray source (and, if it is near enough, as an optical source). Several thermally emitting neutron stars have been observed, some from nearby isolated sources and others from binaries in globular clusters. To a zeroth approximation, thermal emission

from neutron stars is blackbody, so measures of their integrated fluxes and temperatures yield estimates of their angular diameters through Kirchhoff's laws. However, because the observed flux is redshifted twice and the temperature once, the inferred radius is not the geometric radius R but rather the so-called radiation radius: $R_\infty = R/\sqrt{1 - 2GM/Rc^2}$. A significant complication, however, is that the emissions are modulated by a star's atmosphere and magnetic field; a neutron star is not a perfect blackbody.

The principal uncertainties in extracting radii from thermal emissions include the following.

1. The distance D (because the inferred $R_\infty \propto D$).
2. The magnitude of interstellar hydrogen (H) absorption, given that most hard UV radiation and an appreciable fraction of X-rays are absorbed between the star and the Earth.
3. The atmospheric composition and magnetic field strength and distribution.

The best chances of an accurate measurement are from either (*a*) nearby isolated neutron stars for which parallax distances are available (but have unknown atmospheric compositions and field strengths) or (*b*) quiescent X-ray binaries in globular clusters with reliable distances. Due to recent accretion episodes, these sources are believed to have low magnetic fields and, almost certainly, H-dominated atmospheres, which are the most reliably modeled (86).

The best-studied isolated neutron star is RX J1856-3754 (87), which is the only one close enough to have an accurate parallactic distance: $D = 120 \pm 8$ pc (88). Fitting both ROSAT X-ray and optical spectra with nonmagnetic heavy-element atmospheres (89) yields $R_\infty = 16.1 \pm 1.8$ km and redshift $z = 0.37 \pm 0.03$ for this distance. These values lead to $M = 1.86 \pm 0.23\,M_\odot$ and $R = 11.7 \pm 1.3$ km. A later analysis with Chandra data found $z \simeq 0.3$ and $R_\infty \simeq 15.8$ km (90). However, these models predict spectral features that are not observed, and other observations indicate a substantial magnetic field of order 5×10^{12} G. Burwitz et al. (91) and Ho et al. (92) proposed models with a highly magnetized, condensed surface, yielding $R_\infty > 13$ km in the first case and $R_\infty \simeq 14.6 \pm 1.0$ km and $z \simeq 0.22$ in the second, for $D = 120$ pc. Such models require a trace H atmosphere with a finely tuned mass, whose origin is unclear. Ho et al.'s values imply $M = 1.33 \pm 0.09\,M_\odot$ and $R = 11.9 \pm 0.8$ km (errors include only the distance uncertainty). Although the predicted masses of these two approaches differ, the predicted radii are nearly identical.

Many neutron stars are transients in which accretion proceeds intermittently; the accretion episodes are separated by long periods of quiescence. During accretion, compression of matter in the crust induces nuclear reactions (93) that release heat. When the accretion ceases, the heated crust cools and radiates an observable thermal spectrum (94). Accretion is also believed to suppress the surface magnetic field, which seems to be confirmed by the lack of evidence, such as pulsations or cyclotron spectral features, for a magnetic field significant enough to distort the star's spectrum. Because the timescale for heavier nuclei to sink below the photosphere is short, the spectra can be fitted with well-understood unmagnetized H atmosphere models. Modeling can be used to reliably infer the apparent angular emitting area and, possibly, the surface gravity (95), both of which are functions of R and M. **Figure 10** summarizes the probability distributions of M and R for sources in four globular clusters (95, 96).

4.2. Photospheric Radius Expansion Bursts

Type I X-ray bursts are the result of thermally unstable He (or, in some cases, H) ignition in the accreted envelope of a neutron star (97). The ignition generates a thermonuclear explosion that is observed as an X-ray burst with a rapid rise time ($\sim$1 s) followed by cooling decay ($\sim$10–100 s). If the burst is sufficiently luminous, radiation pressure drives surface layers and the photosphere
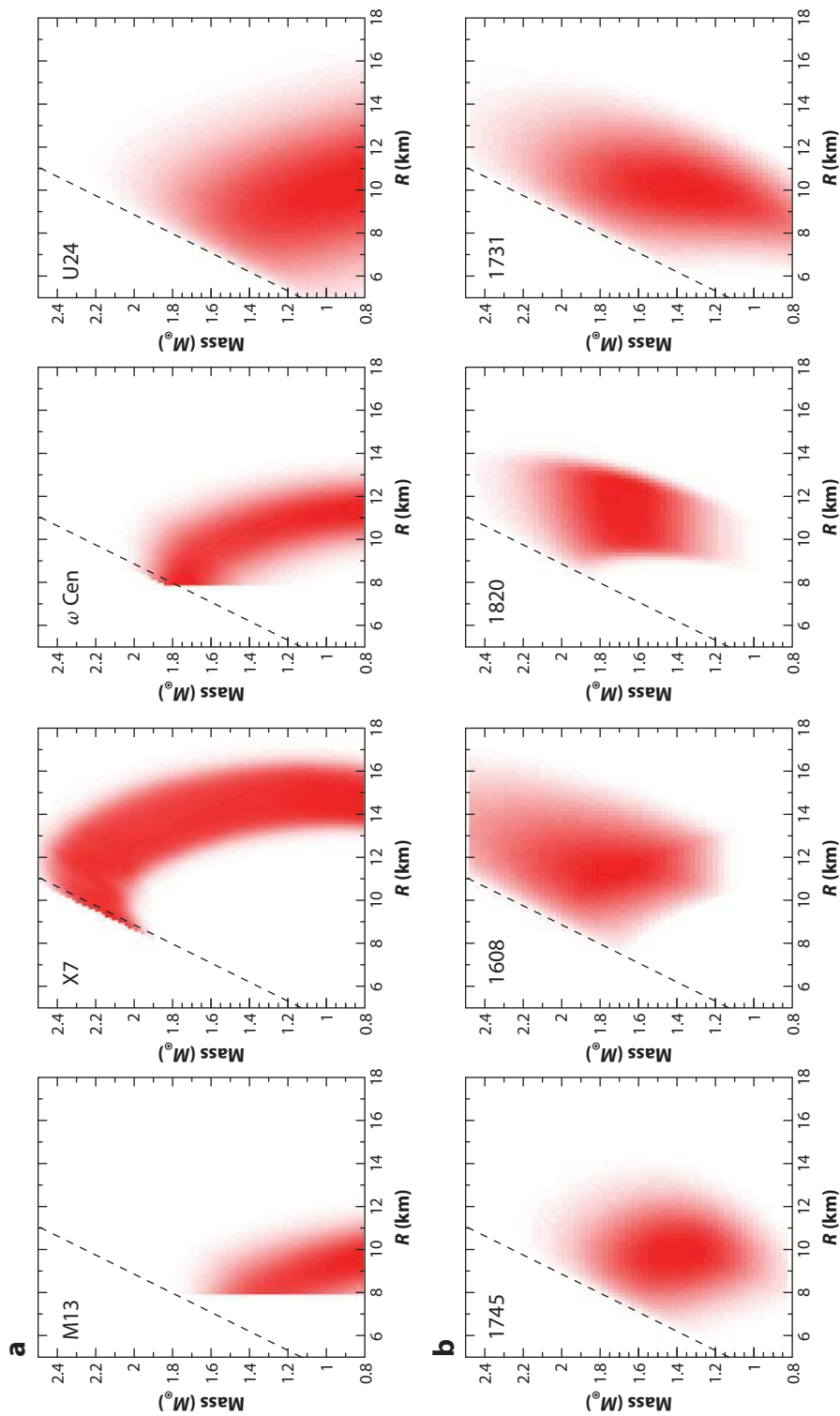
$M-R$ probability densities of neutron stars from (*a*) four quiescent low-mass X-ray binaries in globular clusters and (*b*) four photospheric radius expansion bursts (incorporating the possibility that $R_{\rm ph} > R$). The diagonal lines represent causality limits. Figure reproduced courtesy of A.W. Steiner.

outward to larger radii, and the flux at the photosphere approaches (to within a few percent) the Eddington value,

$$F_{\mathrm{Edd}} = \frac{c\,GM}{\kappa\,D^2}\sqrt{1 - 2\beta_{\mathrm{ph}}}, \qquad\qquad 20.$$

for which radiation pressure balances gravity; the flux then decreases. The opacity of the lifted material is κ, and $\beta_{\mathrm{ph}} = GM/(R_{\mathrm{ph}}c^2)$, where R_{ph} is the radius of the photosphere. The blackbody temperature $T_{\mathrm{bb},\infty}$ also reaches a maximum, marking touchdown as the lifted material falls to the surface. At that time, the observed angular area of the photosphere is

$$A = \frac{F_\infty}{\sigma T_{\mathrm{bb},\infty}^4} = f_c^{-4}\left(\frac{R_{\mathrm{bb},\infty}}{D}\right)^2, \qquad\qquad 21.$$

where f_c is the color-correction factor approximating the effects of the atmosphere in distorting the observed temperature from the effective blackbody temperature. After touchdown, $R_{\mathrm{bb},\infty} = R_{\mathrm{ph}}/\sqrt{1 - 2\beta_{\mathrm{ph}}}$ stabilizes even as the observed flux and temperature decrease. The standard view is that $R_{\mathrm{ph}} = R$; that is, the photosphere lies very close to the surface.

The observed parameters are F_{Edd}, A, and D. Atmosphere models for different compositions and effective temperatures provide κ and f_c. We define

$$\alpha \equiv \frac{F_{\mathrm{Edd}}}{\sqrt{A}}\frac{\kappa D}{c^3 f_c^2} = \beta\sqrt{1 - 2\beta}\sqrt{1 - 2\beta_{\mathrm{ph}}} \qquad\qquad 22.$$

and

$$\gamma \equiv \frac{Ac^3 f_c^4}{F_{\mathrm{Edd}}\kappa} = \frac{R}{\beta(1 - 2\beta)\sqrt{1 - 2\beta_{\mathrm{ph}}}}. \qquad\qquad 23.$$

Note that $\alpha\gamma = R_\infty$. M and R can therefore be determined if α and γ are measured, assuming knowledge of D, κ, and f_c. If $R_{\mathrm{ph}} = R$, then $\alpha = \beta(1 - 2\beta)$, which has two real-valued solutions if $\alpha \leq 1/8$ and none otherwise. The range of γ values for the observed sources is not large.

Özel and collaborators (98, 99) have studied the bursters EXO 1745-248, 4U 1608-522, 4U 1820-30, and KS 1731 and have estimated F_{Edd} and A. Coupled with estimates for D, these authors found $\alpha \simeq 0.13 \pm 0.02$, 0.18 ± 0.06, 0.17 ± 0.02, and 0.21 ± 0.06 respectively. Thus, assuming that $R_{\mathrm{ph}} = R$, no real-valued solutions exist for the centroids of the data. However, real solutions exist in the tails of the error distributions for F_{Edd}, A, and D if one also takes into account theoretical uncertainties in f_c and κ, which are not negligible. Monte Carlo sampling of F_{Edd}, A, D, f_c, and κ within their estimated errors, accepting only trials with real solutions, allows for the generation of probability distributions for M and R. Because requiring real solutions severely restricts the allowed values of input variables, the probability distributions in M and R have smaller errors (of order 5%) than the observational inputs. Another consequence is that the mean values of M and R do not greatly vary from source to source. Relatively small values for the radius ($R \simeq 8 - 10$ km) are found.

The Monte Carlo sampling has extremely small fractional acceptance rates: 0.13, 0.0002, and 2×10^{-8} for the first three of the above sources, for example. This finding casts doubt on the model's validity. Accepted trials are forced into a small region where $\alpha \simeq 1/8$, which, coupled with the fact that γ has an intrinsically small variation among sources, explains the small errors and overlap of M and R values for different sources.

It is likely that this model has systematic uncertainties that have not been considered. One possibility, suggested by Steiner et al. (100), is that the photospheric radius at the point where the Eddington flux is measured might not coincide with the stellar surface. In the extreme case in which $R_{\mathrm{ph}} = \infty$, one has $\alpha = \beta\sqrt{1 - 2\beta}$, which has one physical real-valued solution if $\alpha \leq 3^{-3/2} \simeq 0.192$ and none otherwise. If one allows for the possibility that $R_{\mathrm{ph}} \geq R$, Monte

Carlo acceptance rates increase dramatically (100). Predicted errors for M and R also increase, which leads to 1-σ errors of order 15% (**Figure 10**). Another consequence is that estimated radii are, in each case, approximately 2 km larger than what Özel et al. obtained.

It has been proposed (101), conversely, that the short X-ray bursts used in References 100 and 98 have color-correction factors that change significantly during the burst, which could explain inconsistencies such as the lack of real solutions. By using only long bursts and different model atmospheres, Suleimanov et al. (101) found distinctly larger radii: $R > 14$ km. However, this result is incompatible with studies of nuclei and neutron matter, as discussed in Section 6. This result is also inconsistent with studies of sub-Eddington X-ray bursts from GS 1826-24 (102). Further modeling of X-ray bursts is obviously warranted.

5. FROM OBSERVATIONS TO THE EQUATION OF STATE

With several $M-R$ probability distributions, one can investigate constraints on the overall $M-R$ relation, and the EOS ($p - \varepsilon$ relation) can be inferred by inversion of Equation 2. Steiner et al. (100) assumed a parameterized form for the EOS and determined the most likely parameter values from a Bayesian analysis of the $M-R$ probability distributions by using Markov chain Monte Carlo integration techniques. Below the transition density between the core and crust of a neutron star, $n_{\text{trans}} \simeq n_s/4$, the EOS was assumed to be known because it is dominated by electronic and lattice pressures. In the vicinity of n_s, a standard expansion of the nucleon energy in powers of $n - n_s$ and $1 - 2x$ was assumed, as in Equation 4. The symmetry energy was parameterized as

$$S_2(u) = S_k u^{2/3} + S_p u^\gamma. \qquad 24.$$

The kinetic part of the symmetry energy, $S_k \simeq 13$ MeV, was held fixed, but the compressibility and skewness coefficients, K_o and K_o', and the terms describing the potential part of the symmetry energy, S_p and γ, were taken as parameters.

Above the density ε_1, two polytropic relations with exponents γ_1 and γ_2, separated at the density ε_2, were assumed. Although nuclear masses can establish strong correlations among some parameters, such as those between S_v and γ, these were ignored. The ranges of parameters were constrained to satisfy causality and $M_{\text{max}} > 1.66\,M_\odot$, although raising this limit to $M_{\text{max}} > 1.93\,M_\odot$ in order to comply with observations of J1614-2230 only slightly affects the results (103).

The Bayesian analysis determines the most likely $M-R$ relations (**Figure 11b**) and the most likely values for the EOS parameters. **Figure 11a** displays the most likely ranges for the EOS. 1.4-$M_\odot$ neutron stars are most likely to have radii of order 11.8 ± 0.7 km. These small radii are a consequence of rather soft nuclear symmetry energies: $\gamma = 0.3 \pm 0.1$. Note that the results (89, 92) from spectral modeling of RX J1856-3754 are consistent with the derived $M-R$ relation (**Figure 11**). Although the EOS is relatively soft in the vicinity of ρ_s, the high-density EOS must stiffen: The Bayesian analysis indicates that the neutron star maximum mass is $M_{\text{max}} = 2.05 \pm 0.11\,M_\odot$.

Interestingly, the predicted most-likely values of the three nuclear matter parameters (190 MeV $< K < 260$ MeV, 26 MeV $< S_v < 34$ MeV, and $0.2 < \gamma < 0.4$) are compatible with experimental information. (The skewness K' is neither experimentally nor observationally well constrained.) K is well constrained by monopole resonances to the range 230 MeV $< K < 250$ MeV (see Reference 104 for a review). The symmetry parameters are also consistent with experimental information (see Section 6). There appears to be a remarkable convergence between experimental and astrophysical estimates for the neutron star EOS.

These estimates were made on the basis of relatively poor radius-mass information from only seven to eight neutron stars. These results are somewhat sensitive to how photospheric radius
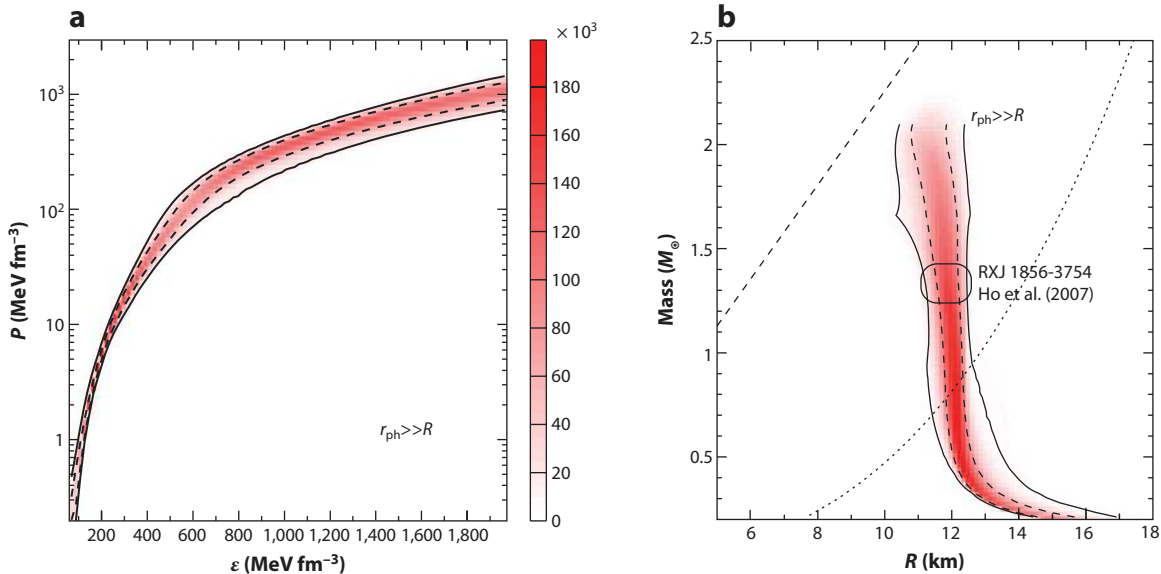
Figure 11

(*a*) Probability distributions for pressure as a function of energy density using the $M-R$ probability distributions from **Figure 10**. (*b*) Probability distributions for the $M-R$ curve. The diagonal dashed line is the causality limit, and the dotted curve is the 716-Hz rotation constraint. 1-σ and 2-σ contours are shown as dashed and solid lines, respectively. Also shown is the estimated mass and radius error region, including only distance errors, for RX J1856-3754 (92). Figure adapted from Reference 100.

expansion bursts are modeled. On the one hand, if one assumes $R_{ph} = R$, the predicted radii from burst sources would become ∼2 km smaller (99); however, in this case, the M_{max} constraint from PSR J1614-2230 can barely be satisfied (100). On the other hand, if the burst data are excluded, the inferred $M-R$ relation is essentially unaltered from the baseline results achieved by incorporating the burst sources with the possibility that $R_{ph} \geq R$ (A.W. Steiner, private communication). In this case, the observed $M-R$ results are largely a consequence of the wide range of observed R_∞ values of the quiescent globular cluster sources (**Figure 10**), which forces the $M-R$ trajectory to enter its vertical trajectory at relatively small radii (∼12 km). Otherwise, the existence of both small and large observed values of R_∞ would not be compatible with realistic masses.

$M-R$ information has also been inferred from pulse-shape modeling of X-ray bursts. Although predictions from observations of individual sources have large errors, Leahy et al. (105) conclude that only an $M-R$ curve with a constant radius of 12 km for $1\,M_\odot < M < 2.3\,M_\odot$ would be consistent with observations of all sources studied, namely XTE J1807-294, SAX J1808-3658, and XTE J1814-334. Such a result is remarkably similar to the conclusions drawn in Reference 100 (**Figure 11**).

Nevertheless, Suleimanov et al.'s (101) study of longer X-ray bursts implies considerably larger radii: $R \gtrsim 14$ km. Those results are further supported by spin-phase-resolved spectroscopy of isolated neutron stars (106) that yield small neutron star redshifts: $z \simeq 0.16$. This value for z, coupled with $M > 1.2\,M_\odot$, implies that $R > 14$ km. Because these results are also incompatible with available experimental information discussed in the next section, it is important to resolve these differences. More sophisticated modeling of photospheric radius expansion bursts and neutron star atmospheres, together with refinements of distances, will be required for additional progress.

6. LABORATORY CONSTRAINTS

The most significant aspects of neutron star structure impacted by the EOS are the maximum mass and the typical radius of intermediate stars. The former is mostly sensitive to the EOS beyond three times the saturation density. **Figure 3** shows that this density is the minimum central density of stars greater than approximately $1.5\,M_\odot$, whereas the central densities at the maximum mass can approach $7 - 8\,n_s$. However, the radii of stars with mass $\lesssim 1.5\,M_\odot$ are completely determined by the EOS below $3n_s$ and, in particular, by dS/du in the vicinity of n_s.

6.1. Nuclear Symmetry Energy

The nuclear symmetry energy $S(u)$ is often described by the liquid droplet parameters,

$$
\begin{aligned}
S_v &= S_2(1), \\
L &= \frac{3}{8}u\left(\frac{\partial^3 e}{\partial u \partial^2 x}\right)_{u=1,x=1/2} = 3u\left(\frac{dS_2}{du}\right)_{u=1}, \\
K_{\text{sym}} &= \frac{9}{8}u^2\left(\frac{\partial^4 e}{\partial u^2 \partial^2 x}\right)_{u=1,x=1/2} = 9u^2\left(\frac{d^2 S_2}{du^2}\right)_{u=1}.
\end{aligned}
\qquad 25.
$$

For example, in the parameterization of Equation 24, $L = 2S_k + 3\gamma(S_v - S_k)$ and $K_{\text{sym}} = -2S_k + 9\gamma(\gamma - 1)(S_v - S_k)$. There are limited constraints from measurements of the giant isoscalar monopole resonance (107), isotopic transport ratios in medium-energy heavy-ion collisions (108), and neutron skin data from antiprotonic atoms (109). However, extraction of the symmetry contribution to the total incompressibility of nuclei and its separation into bulk (K_{sym}) and surface contributions is still problematic.

In contrast, there are several methods of experimentally determining S_v and L, including (*a*) nuclear mass fitting, (*b*) neutron skin thickness, (*c*) dipole polarizabilities, (*d*) dynamics in heavy-ion collisions, (*e*) giant and pygmy dipole resonances, and (*f*) isobaric analog states. The most accurate data are obtained from fitting nuclear masses. However, optimizing the symmetry parameters of nuclear models to experimental masses cannot uniquely constrain them. Rather, the parameters are highly correlated (110–114).

It is straightforward to demonstrate the existence of this correlation by use of the liquid drop model (115). Although the specific results are sensitive to the inclusion of shell and pairing terms, Coulomb diffusion and exchange terms, a Wigner term, and the neutron skin, these effects are inconsequential for this demonstration. Neglecting these contributions, the symmetry energy of a nucleus to lowest order is $E_{\text{mod},A} = I^2(S_v A - S_s A^{2/3})$, where $I = (N - Z)/(N + Z)$, and consists of a volume term and a surface term. The volume parameter S_v is the same as the bulk parameter in Equation 26. S_s is the surface symmetry energy parameter, which is sensitive to the density dependences of both e and S and thus depends on both S_v and L. Minimizing the difference between the model and experimental symmetry energies for nuclei with measured masses—that is, $\chi^2 = \sum_i (E_{\text{exp},i} - E_{\text{mod},i})^2/(\mathcal{N}\sigma^2)$, where $\mathcal{N}$ is the total number of nuclei and σ is a nominal error—establishes a correlation between S_v and S_s. This correlation can be visualized as a 1-σ confidence ellipse: a χ^2 contour that is one unit larger than the minimum value of χ^2. The shape and orientation of this ellipse are determined by the second derivatives of χ^2 at the minimum,

$$
[\chi_{vv}, \chi_{vs}, \chi_{ss}]\sigma^2 = \frac{2}{\mathcal{N}}\sum_i I_i^4[A_i^2, -A_i^{5/3}, A_i^{4/3}] \simeq [61.6, -10.7, 1.87], \qquad 26.
$$

where $\chi_{vs} = \partial^2\chi^2/\partial S_v \partial S_s$, and so on. In the simple liquid drop case, these derivatives do not depend on the location of the minimum. The confidence ellipse has an orientation

$\alpha = (1/2)\tan^{-1}|2\chi_{vs}/(\chi_{vv} - \chi_{ss})| \simeq 9.8°$ with respect to the S_s axis; the ellipse's semimajor axes are the error widths, $\sigma_v = \sqrt{(\chi^{-1})_{vv}} \simeq 2.3$ MeV and $\sigma_s = \sqrt{(\chi^{-1})_{ss}} \simeq 13.2$ MeV, where (χ^{-1}) is the matrix inverse and we use $\sigma = 1$ MeV.

To convert the correlation between S_s and S_v into a correlation between L and S_v, one needs to estimate how S_s depends on S_v and L. Treating the nuclear surface as a plane-parallel interface, S_s can be expressed simply as the ratio of two integrals over the nuclear density $u = n/n_s$ of a symmetric system (112, 113, 116):

$$S_s = \frac{E_s S_v}{2} \frac{\int_0^1 u^{1/2}[S_v/S_2(u) - 1][e(u, 1/2) + B]^{-1/2}du}{\int_0^1 u^{1/2}[e(u, 1/2) + B]^{1/2}du}. \qquad 27.$$

Here, $E_s \simeq 19$ MeV is the liquid drop surface energy parameter (also found from fitting nuclear masses). The solution depends on the functional forms of S and e and is generally nontrivial, but an analytical result is found if we approximate $S_2(u) \simeq S_v + L(u - 1)/3$ and $e(u, 1/2) + B \simeq K(u - 1)^2/18$:

$$\frac{S_s}{S_v} \simeq \frac{135 E_s}{2K}\left[1 - \left[\frac{3S_v}{L} - 1\right]^{1/2}\tan^{-1}\left(\left[\frac{3S_v}{L} - 1\right]^{-1/2}\right)\right]. \qquad 28.$$

For example, for $L/(3S_v) \simeq 1/3$, $1/2$, or $2/3$, one finds $S_s/S_v \simeq 0.7$, 1.2, or 1.8, which shows the basic trend. For various interactions constrained to broadly reproduce nuclear masses in Hartree–Fock or Thomas–Fermi calculations, an approximate relation can be found (117):

$$\frac{S_s}{S_v} \simeq 0.646 + \frac{S_v}{97.9 \text{ MeV}} + 0.436\frac{L}{S_v} + 0.0873\left(\frac{L}{S_v}\right)^2. \qquad 29.$$

By transforming to $S_v - L$ space, one finds that the confidence ellipse in $S_v - L$ space has $\sigma_v \simeq 2.3$ MeV and $\sigma_L \simeq 20$ MeV.

In practice, the liquid droplet model (118), which accounts for varying neutron-to-proton ratios within the nucleus, provides an improved fit to nuclear masses. Its symmetry energy is $E_{\text{mod},A} = I_i^2 S_v A(1 + S_s A^{-1/3}/S_v)^{-1}$, and the above methodology can be used to determine the confidence ellipse. One finds $\sigma_v \simeq 3.1$ MeV and $\sigma_L \simeq 47$ MeV (these values now depend on the location of the minimum, $S_{v0} \simeq 30.5$ MeV, and $L_0 \simeq 62$ MeV).

Modern microscopic models of nuclei are a vast improvement over liquid drop and droplet models. Nevertheless, they predict an $S_v - L$ correlation in substantial agreement with the liquid droplet model or Thomas–Fermi calculations (111, 117). The correlation was recently studied by Kortelainen et al. (114), who used the universal nuclear energy density functional (119). Fitting nuclear masses and charge radii and arbitrarily assuming $\sigma = 2$ MeV resulted in a confidence ellipse with the properties $S_{v0} \simeq 30.5$ MeV, $L_0 \simeq 45$ MeV, $\sigma_v = 3.1$ MeV, and $\sigma_L = 40$ MeV, and an orientation that is indistinguishable from that predicted by the liquid droplet model and Thomas–Fermi calculations. The correlation of these parameters was more than 97%, which is illustrated in **Figure 12** for the 90%-confidence contour. Also, the latest microscopic finite-range droplet model (120), when optimized to nuclear masses, predicted best-fit values of $S_{v0} \simeq 32.5$ MeV and $L_0 \simeq 70$ MeV. This result lies precisely on the Kortelainen et al. correlation line with their confidence ellipse (**Figure 12**). This correlation is therefore robust and model independent.

This correlation has been used to constrain nuclear parameters in supernova simulations that explored the effects of variations in the nuclear symmetry energy (121). Coupled with other nuclear observables, this correlation can become even more effective. One possibility concerns the neutron skin thickness of neutron-rich nuclei. Neglecting Coulomb effects, the difference
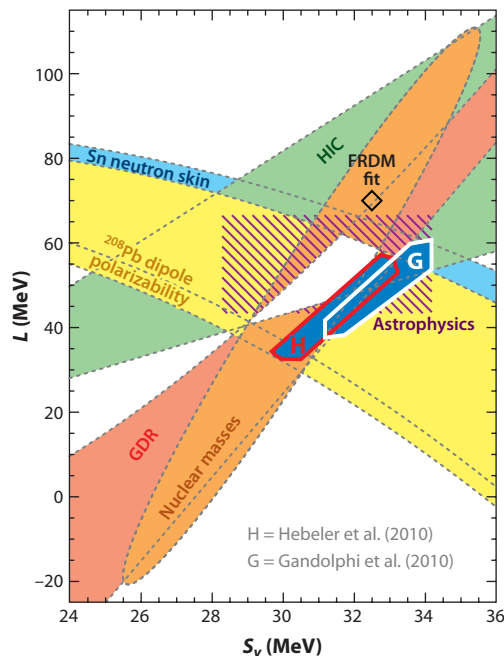
Figure 12

Summary of constraints on symmetry energy parameters. The filled ellipsoid indicates joint $S_v - L$ constraints from nuclear masses (114). The finite-range droplet model fit (120) is indicated with a diamond. The filled bands show constraints from neutron skin thickness of tin (Sn) isotopes (122), isotope diffusion in heavy-ion collisions (HIC) (124), the dipole polarizability of ^{208}Pb (126), and giant dipole resonances (GDR) (128). The hatched rectangle shows constraints from astrophysical modeling of $M-R$ observations (100). The two closed curves show neutron matter constraints (H is from Reference 134, and G is from Reference 135.) The white area is the experimentally allowed overlap region. Adapted from Reference 117.

between the mean neutron and proton surfaces in the liquid droplet model (118) is

$$t_{np} = \frac{2r_o}{3} \frac{S_s I}{S_v + S_s A^{-1/3}}. \qquad 30.$$

Therefore, neglecting Coulomb effects, the neutron skin thickness of any particular isotope is predicted to be primarily a function of S_s/S_v, and hence, through Equation 29, L/S_v. Values of t_{np} have been measured, typically with 30–50% errors, for approximately two dozen isotopes. A recent study (122) fitting the neutron skin thicknesses of tin isotopes, in which differential measurements reduce errors, found a correlation between S_v and L that is nearly orthogonal to the mass-fit correlation (**Figure 12**). Additionally, neutron skin measurements of antiprotonic atoms yield a range between 25 MeV and 70 MeV (109) for L (which is consistent with the tin study but for clarity is not shown in **Figure 12**). The first results (123) from the PREX experiment to measure the neutron skin of ^{208}Pb have indicated a limit of 35 MeV < L < 262 MeV. The mean value is discrepant with other results for neutron skins, but the errors are still very large.

Figure 12 shows an additional constraint from isospin diffusion in heavy-ion collisions (124). Tamii et al. (125) established a constraint from measurements of the dipole polarizability of ^{208}Pb, and a later study by Piekarewicz et al. (126), who attempted a more model-independent analysis, obtained the constraint shown in **Figure 12**. A related experimental constraint originates from measurements of the centroids of giant dipole resonances in spherical nuclei. The hydrodynamical

model from Reference 127 showed that both the dipole polarizability and the giant dipole centroid energy are closely connected to liquid droplet parameters. For example, the centroid energy is

$$E_{-1} \simeq \sqrt{\frac{3\hbar^2}{m < r^2 >} S_v \left(1 + \frac{5}{3} \frac{S_s}{S_v} A^{-1/3} \right)^{-1} (1 + \kappa)},$$ 31.

where κ is an enhancement factor arising from the velocity dependence of the interaction and $<r^2>$ is the mean-square radius. The factor $m<r^2>(1 + \kappa)$ does not significantly vary among interactions for a given nucleus. By using various Skyrme functions to fit the centroid energy in ^{208}Pb, Trippa et al. (128) showed that Equation 31 is approximately equivalent to evaluating $S(u)$ at the subnuclear density 0.1 fm^{-3}, which leads to a small range 23.3 MeV $< S_{0.1} <$ 24.9 MeV. Although the relation among $S_{0.1}$, S_v, and L is model dependent, bounds (117) for a range of parameterizations are indicated with the constraint band shown in **Figure 12**.

A study of pygmy dipole resonances (129) in ^{68}Ni and ^{132}Sn imply that 31 MeV $< S_v <$ 33.6 MeV and 49.1 MeV $< L <$ 80 MeV. However, Daoutidis & Goriely (130) claim that both theoretical and experimental uncertainties prevent them from being effective constraints, which is supported by the results from Reinhard & Nazarewicz (131) that show a lack of correlation with L. This constraint is not shown in **Figure 12**.

Danielewicz & Lee (132) proposed isobaric analog states as constraints on symmetry parameters, leading to $S_v \simeq 32.9$ MeV and $S_s \simeq 96$ MeV, which are equivalent to $L \simeq 113$ MeV. However, the data suggest that there could be a significant curvature contribution; refitting with curvature yields $S_v \sim 30$ MeV and $S_s \sim 45$ MeV, which are equivalent to $L \sim 50$ MeV, but with considerable errors. A more detailed analysis will be necessary to produce better constraints. Further constraints on L alone were suggested from multifragmentation in intermediate-energy heavy-ion collisions (126), leading to 40 MeV $< L <$ 125 MeV. Although consistent with other constraints, neither result is useful for further restricting parameter space.

Most of the experimental studies discussed above have a remarkable consistency. The white overlap region in **Figure 12** shows the common predictions of the experimental studies (note that the finite-range droplet model would also predict a confidence ellipse similar in extent and orientation to that of Reference 114, but this was not calculated). It is remarkable that the overlap is fully consistent with the observational inferences made in Reference 100.

6.2. Neutron Matter and High-Density Constraints

The symmetry parameters are also related to properties of pure neutron matter at the saturation density. If quartic and higher terms in the symmetry energy expansion can be neglected, the energy and pressure of pure neutron matter at n_s are given by Equations 4 and 5 as $e_{n_s} = S_v - B$ and $p_{n_s} = Ln_s/3$, respectively. However, depending on the nuclear interaction, this might not be a good approximation. Considering only the nonrelativistic, noninteracting kinetic energy contributions, the errors made using the quadratic approximation are

$$e_{n_s,k} - S_k + B = \left(\frac{3}{5} 2^{2/3} - \frac{1}{3} \right) \frac{\hbar^2}{2m_b} \left(\frac{3\pi^2 n_s}{2} \right)^{2/3} \equiv Q \simeq 0.72\,\text{MeV},$$
$$\frac{p_{n,k}}{n_s} - \frac{L_k}{3} = \frac{2}{3} Q \simeq 0.96\,\text{MeV}.$$ 32.

Although these differences are not large, contributions from the effective mass and potential energy contributions can be considerably larger, and the errors amplify at high densities (133). Therefore, one should take care in relating S_v and L to neutron matter properties.

Two recent independent studies (134, 135) have estimated properties of neutron matter based on chiral Lagrangian and quantum Monte Carlo techniques with realistic two- and three-nucleon
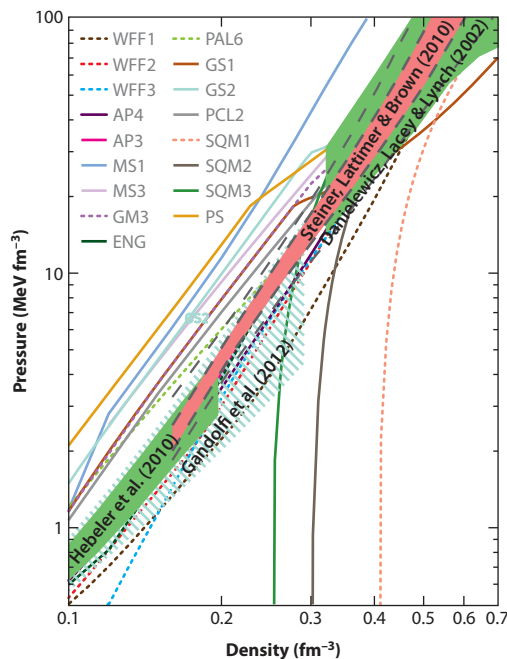
Figure 13

Representative hadronic and strange quark matter (SQM) equations of state, as in **Figure 2** but with astrophysical results (100), neutron matter calculations (134, 135), and heavy-ion studies (136) overlaid.

interactions. Employing realistic ranges of the magnitudes of these interactions, and neglecting quartic and higher symmetry contributions, the neutron matter studies lead to the ranges shown in **Figure 12** (128, 129). The close agreement between neutron matter studies and laboratory constraints is encouraging, although the caveat regarding the neglect of quartic and higher terms in the symmetry expansion should be kept in mind. However, given that neutron star matter and pure neutron matter differ by relatively minor amounts because $x \ll 1$, the comparison between the neutron matter and astrophysics results does not have the ambiguity inherent in the comparisons with laboratory data. In fact, the agreement with astrophysical data is very good, not only for the derived symmetry parameters but also for the overall pressure-density relation at moderate densities (**Figure 13**).

There is a paucity of experimental information concerning the EOS at densities modestly exceeding n_s. Danielewicz et al. (136) analyzed the elliptic and transverse flows of matter in heavy-ion (Au-Au) collisions to estimate the pressure as a function of density in the range from 2 to 5 n_s. However, the conditions of interest involve large excitation energies and nearly symmetric matter. The inferred pressures and energy densities must therefore be extrapolated to zero temperature and to large neutron excesses that are characteristic of neutron star matter. Doing so introduces considerable systematic errors. Nevertheless, the results (**Figure 13**) also compare favorably with the astrophysical constraints (100).

7. CONCLUSIONS

An ever-increasing set of astrophysical data concerning neutron star masses and radii has placed severe constraints on the nuclear EOS. The available data suggest that neutron stars of canonical

mass $1.4\,M_\odot$ have radii near 11.5 km, which strongly implies that the EOS near the nuclear saturation density is relatively soft—in other words, that the pressure there is relatively low. At the same time, the EOS must stiffen at densities exceeding 2 to $3n_s$ to permit the existence of $2\text{-}M_\odot$ neutron stars. Although the existence of exotic matter such as deconfined quarks, kaon condensates, and hyperons in neutron star interiors are not excluded by these considerations, their role in the pressure-density relation must not be great. There are hints that even more massive neutron star masses are waiting to be discovered. The detection of neutron stars with approximately $2.4\,M_\odot$ would be exciting because of the potential to rule out the existence of some types of exotic matter. Even if the existence of such massive neutron stars is not confirmed, the presence of exotic matter may yet be revealed by observations of cooling neutron stars (8).

The detection of gravitational radiation from mergers involving neutron stars will present additional opportunities. With an expected detection rate of 0.4 to 40 neutron stars per year with Advanced LIGO (137), many new mass and radius estimates will become available. Given the observed narrow mass range of double–neutron star binaries, observations of the peak frequency may also yield radius measurements with an accuracy of 0.1 km (138). Furthermore, if the events are nearby enough, observations of postmerger gravitational waves could set interesting upper limits to the neutron star maximum mass.

The conclusions regarding the mass-radius relation and the nuclear symmetry energy from astrophysical observations of quiescent neutron stars in globular clusters and from type I X-ray bursts are strongly supported by the convergence in the predicted properties of dense matter, as revealed by nuclear experiments and theoretical neutron matter calculations. Although the symmetry parameters S_v and L do not completely describe the extrapolation from symmetric matter to neutron-rich matter, it is gratifying that their permissible ranges are now reasonably restricted, as shown in **Figure 12**: $29.0\,\text{MeV} < S_v < 32.5\,\text{MeV}$, and $41\,\text{MeV} < L < 60\,\text{MeV}$. Continuing astrophysical observations combined with experimental studies of giant dipole resonances and dipole polarizabilities, as well as neutron skins, have great potential to further improve these constraints.

DISCLOSURE STATEMENT

The author is not aware of any affiliations, memberships, funding, or financial holdings that might be perceived as affecting the objectivity of this review.

ACKNOWLEDGMENTS

LITERATURE CITED

1. Manchester RN, Hobbs GB, Teoh A, Hobbs M. *Astron. J.* 129:1993 (2005)
2. Weisberg JM, Nice DJ, Taylor JH. *Astrophys. J.* 722:1030 (2010)
3. Kramer M, et al. *Science* 314:97 (2006)
4. Bionta RM, et al. *Phys. Rev. Lett.* 58:1494 (1987); Hirata K, et al. *Phys. Rev. Lett.* 58:1490 (1987)
5. Lattimer JM, Yahil A. *Astrophys. J.* 340:426 (1989)
6. Bauswein A, Janka H-T. *Phys. Rev. Lett.* 108:1101 (2012); Lackey BD, et al. *Phys. Rev. D* 85:044061 (2012)

7. Lattimer JM, van Riper KA, Prakash M, Prakash M. *Astrophys. J.* 425:802 (1994); Gnedin OY, Yakovlev DG, Potekhin AY. *Mon. Not. R. Astron. Soc.* 324:725 (2001)

8. Page D, Lattimer JM, Prakash M, Steiner AW. *Astrophys. J.* 707:1131 (2009); Yakovlev DG, Pethick CJ. *Annu. Rev. Astron. Astrophys.* 42:169 (2004)

9. Oppenheimer JR, Volkoff GM. *Phys. Rev.* 55:374 (1939)

10. Chodos A, et al. *Phys. Rev. D* 9:3741 (1974)

11. Haensel P, Zdunk JL, Douchin F. *Astron. Astrophys.* 385:301 (2002)

12. Page D, Prakash M, Lattimer JM, Steiner AW. *Phys. Rev. Lett.* 85:2048 (2000)

13. Lattimer JM, Prakash M. *Astrophys. J.* 550:426 (2001)

14. Hessels JWT, et al. *Science* 311:1901 (2006)

15. Lattimer JM, Prakash M. *Phys. Rep.* 442:109 (2007)

16. Koranda S, Stergiolas N, Friedman JL. *Astrophys. J.* 488:799 (1997)

17. Lindblom L. *Astrophys. J.* 278:364 (1984)

18. Rhoades CE Jr, Ruffini R. *Phys. Rev. Lett.* 32:324 (1974)

19. Lattimer JM, Prakash M. *Phys. Rev. Lett.* 94:1101 (2005)

20. Tolman RC. *Phys. Rev.* 55:364 (1939)

21. Lattimer JM, Prakash M. *Science* 304:536 (2004); Haensel P, Zdunik JL, Bejger M, Lattimer JM. *Astron. Astrophys.* 502:605 (2009)

22. Lattimer JM, Prakash M. In *From Nuclei to Stars*, ed. S Lee, p. 275. Singapore: World Sci. (2011)

23. Manchester RN, Taylor JH. *Pulsars.* San Francisco: WH Freeman (1977)

24. Shapiro II. *Phys. Rev. Lett.* 13:789 (1964)

25. Damour T, Deruelle N. *Ann. Inst. Henri Poincaré Phys. Theor.* 44:263 (1986); Freire PCC, Wex N. *Mon. Not. R. Astron. Soc.* 409:199 (2010)

26. Tauris TM, Savonije GJ. *Astron. Astrophys.* 350:928 (1999)

27. Janssen GH, et al. *Astron. Astrophys.* 490:753 (2008)

28. Gonzalez ME, et al. *Astrophys. J.* 743:102 (2011)

29. Arzoumanian Z, Joshi K, Rasio F, Thorsett SE. *Astron. Soc. Pac. Conf. Ser.* 105:525 (1996)

30. Lynch RS, Freire PCC, Ransom SM, Jacoby BA. *Astrophys. J.* 745:109 (2012)

31. Thorsett SE, Chakrabarty D. *Astrophys. J.* 512:288 (1999)

32. Clark JS, et al. *Astron. Astrophys.* 392:909 (2002)

33. Rawls ML, et al. *Astrophys. J.* 730:25 (2011)

34. Casares J, González Hernández JI, Israelian G, Rebolo R. *Mon. Not. R. Astron. Soc.* 401:2517 (2010)

35. Gelino DM, Tomsick JA, Heindl WA. *Bull. Am. Astron. Soc.* 34:1199 (2003)

36. Steeghs D, Jonker PG. *Astrophys. J. Lett.* 669:85 (2007)

37. Muñoz-Darias T, Casares J, Martínez-Pais IG. *Astrophys. J.* 635:520 (2005)

38. Mason AB, et al. *Astron. Astrophys.* 509:79 (2010)

39. van Kerkwijk MH, Breton R, Kulkarni SR. *Astrophys. J.* 728:95 (2011)

40. Mason AB, et al. *Astron. Astrophys.* 532:A124 (2011)

41. Mason AB, et al. *Astron. Astrophys.* 422:199 (2005)

42. Champion DJ, et al. *Mon. Not. R. Astron. Soc.* 363:929 (2005)

43. Corongiu A, et al. *Astron. Astrophys.* 462:703 (2007)

44. Kasian L. *AIP Conf. Ser.* 983:487 (2008)

45. Stairs IH, Thorsett SE, Taylor JH, Wolszczan A. *Astrophys. J.* 581:501 (2002)

46. Weisberg JM, Nice DJ, Taylor JH. *Astrophys. J.* 722:1030 (2010)

47. Jacoby BA, et al. *Astrophys. J. Lett.* 644:113 (2006)

48. Kramer M, et al. *Science* 314:97 (2006)

49. Ferdman RD. *Binary pulsar systems: environments and evolution.* PhD thesis, Univ. B.C. 227 pp. (2008)

50. Lange C, et al. *Mon. Not. R. Astron. Soc.* 326:274 (2001)

51. Splaver EM, et al. *Astrophys. J.* 620:405 (2005)

52. Nice DJ, Splaver EM, Stairs IH. *Astron. Soc. Pac. Conf. Ser.* 302:75 (2003)

53. Nice DJ, Stairs IH, Kasian LE. *AIP Conf. Proc.* 983:453 (2008)

54. Verbiest JPW, et al. *Astrophys. J.* 679:675 (2008)

55. Bhat NDR, Bailes M, Verbiest JPW. *Phys. Rev. D* 77:124017 (2008)

56. Kiziltan B, Kottas A, Thorsett SE. arXiv:1011.4291v1 [astro-ph] (2011)
57. Hotan AW, Bailes M, Ord SM. *Mon. Not. R. Astron. Soc.* 369:1502 (2006)
58. Ferdman RD, et al. *Astrophys. J.* 711:764 (2010)
59. Freire PCC, Wolszcan A, van den Berg M, Hessels JWT. *Astrophys. J.* 679:1433 (2008)
60. Freire PCC, et al. *Astrophys. J.* 675:670 (2008)
61. Antoniadis J, et al. *Mon. Not. R. Astron. Soc.* In press (2012)
62. Bassa CG, van Kerkwijk MH, Koester D, Verbunt F. *Astron. Astrophys.* 456:295 (2006)
63. Demorest PB, et al. *Nature* 467:1081 (2010)
64. Guillemot L, et al. *Mon. Not. R. Astron. Soc.* 422:1294 (2012)
65. Nice DJ, Splaver EM, Stairs IH. *Astrophys. J.* 549:516 (2001)
66. Nice DJ. *Astrophys. J.* 549:516 (2001)
67. Freire PCC, et al. *Mon. Not. R. Astron. Soc.* 412:2763 (2011)
68. Ransom SM, et al. *Science* 307:892 (2005)
69. Reynolds MT, et al. *Mon. Not. R. Astron. Soc.* 379:1117 (2007)
70. Özel F, Psaltis D, Narayan R, Villarreal AS. arXiv:1201:1006 [astro-ph] (2012)
71. Nomoto K. *Astrophys. J.* 277:791 (1984); Nomoto K. *Astrophys. J.* 322:206 (1987)
72. Burrows A, Lattimer JM. *Astrophys. J.* 307:178 (1986)
73. Strobel K, Schaab C, Weigel MK. *Astron. Astrophys.* 350:497 (1999)
74. Zhang CM, et al. *Astron. Astrophys.* 527:A83 (2011)
75. Schwab J, Podsiadlowski P, Rappaport S. *Astrophys. J.* 719:722 (2010)
76. Knigge C, Coe JJ, Podsiadlowski P. *Nature* 479:372 (2011)
77. Podsiadlowski P, et al. *Mon. Not. R. Astron. Soc.* 361:1243 (2005)
78. Mereghetti S. In *High-Energy Emission from Pulsars and Their Systems*, ed. N Rea, DF Torres, p. 345. Berlin: Springer (2011)
79. Lewin WHG, van Paradijs J, Taam RE. *Space Sci. Rev.* 62:223 (1993)
80. Miller MC. *Adv. Space Res.* 38:2680 (2006)
81. Lattimer JM, Schutz B. *Astrophys. J.* 629:979 (2005)
82. Link B, Epstein RI, Lattimer JM. *Phys. Rev. Lett.* 83:3362 (1999)
83. Cackett EM, et al. *Mon. Not. R. Astron. Soc.* 372:479 (2006)
84. Samuelsson L, Anderson N. *Mon. Not. R. Astron. Soc.* 374:256 (2006)
85. Leahy DA, et al. *Astrophys. J.* 691:1235 (2009)
86. Rutledge RE, et al. *Astrophys. J.* 514:945 (1999)
87. Walter FM, Wolk SJ, Neuhäuser R. *Nature* 379:233 (1996)
88. Walter FM, et al. *Astrophys. J.* 724:669 (2010); Walter FM, Lattimer JM. *Astrophys. J.* 576:145 (2002)
89. Pons JA, et al. *Astrophys. J.* 564:981 (2002)
90. Walter FM. *J. Phys. G* 30:S461 (2004)
91. Burwitz V, et al. *Astron. Astrophys.* 399:1109 (2003)
92. Ho WCG, et al. *Mon. Not. R. Astron. Soc.* 375:821 (2007)
93. Haensel P, Zdunik JL. *Astron. Astrophys.* 227:431 (1990)
94. Brown EF, Bildsten L, Rutledge RE. *Astrophys. J.* 504:L95 (1998)
95. Heinke CO, Rybicki GB, Narayan R, Grindlay JE. *Astrophys. J.* 644:1090 (2006)
96. Webb NA, Barret D. *Astrophys. J.* 671:727 (2007); Guillot S, Rutledge RE, Brown EF. *Astrophys. J.* 732:88 (2011)
97. Strohmayer TE, Bildsten L. In *Compact Stellar X-Ray Sources*, ed. W Lewin, M van der Klis, p. 113. Cambridge, UK: Cambridge Univ. Press (2004)
98. Özel F, Güver T, Psaltis D. *Astrophys. J.* 693:1775 (2009); Güver T, Özel F, Cabrera-Lavers A. *Astrophys. J.* 712:964 (2010); Güver T, Wroblewski P, Camarota L, Özel F. *Astrophys. J.* 719:1807 (2010); Özel F, Gould A, Güver T. *Astrophys. J.* 748:5 (2012)
99. Özel F, Baym G, Güver T. *Phys. Rev. D* 82:1301 (2010)
100. Steiner AW, Lattimer JM, Brown EF. *Astrophys. J.* 722:33 (2010)
101. Suleimanov V, Poutanen J, Revnivstev M, Werner K. *Astrophys. J.* 742:122 (2011)
102. Zamfir M, Cumming A, Galloway DK. *Astrophys. J.* 749:69 (2012)
103. Steiner AW, Gandolfi S. *Phys. Rev. Lett.* 108:081102 (2012)

104. Piekarewicz J. *J. Phys. G* 37:064308 (2010)
105. Leahy DA, Morsink SM, Chou Y. *Astrophys. J.* 742:17 (2011)
106. Hambaryan V, et al. *Astron. Astrophys.* 534:74 (2011)
107. Li T, et al. *Phys. Rev. C* 81:034309 (2010)
108. Chen L-W, et al. *Phys. Rev. C* 80:041322 (2009)
109. Centelles M, Roca-Maza X, Viñas X, Warda M. *Phys. Rev. Lett.* 102:122502 (2009); Warda M, Viñas X, Roca-Maza X, Centelles M. *Phys. Rev. C* 80:024316 (2009)
110. Lattimer JM. In *The Structure and Evolution of Neutron Stars*, ed. D Pines, R Tamagaki, S Tsuruta, p. 50. New York: Addison-Wesley (1992); Lattimer JM. In *Nuclear Equation of State*, ed. A Ansari, L Satpathy, p. 83. Singapore: World Sci. (1996)
111. Oyamatsu K, Iida K. *Nucl. Phys. A* 718:38 (2003)
112. Danielewicz P. *Nucl. Phys. A* 727:233 (2003)
113. Steiner AW, Prakash M, Lattimer JM, Ellis PJ. *Phys. Rep.* 411:325 (2005)
114. Kortelainen M, et al. *Phys. Rev. C* 82:4313 (2010)
115. von Weizsäcker CF. *Z. Phys.* 96:431 (1935)
116. Krivine H, Treiner J. *Phys. Lett. B* 124:127 (1983)
117. Lim Y, Lattimer JM. arXiv:1203.4286 [nucl-th] (2012)
118. Myers WD, Swiatecki WJ. *Ann. Phys.* 55:395 (1969)
119. Bertsch DF, Dean DJ, Nazarewicz W. *SciDAC Rev.* 6:42 (2007)
120. Moller P, Myers WD, Sagawa H, Yoshida S. *Phys. Rev. Lett.* 108:052501 (2012)
121. Swesty FD, Lattimer JM, Myra ES. *Astrophys. J.* 425:195 (1994)
122. Chen L-W, Ko CM, Li B-A, Xu J. *Phys. Rev. C* 82:024321 (2010)
123. Abrahamyan S, et al. *Phys. Rev. Lett.* 108:112502 (2012)
124. Tsang MB, et al. *Phys. Rev. Lett.* 102:122701 (2009)
125. Tamii A, et al. *Phys. Rev. Lett.* 107:062502 (2008)
126. Piekarewicz J, et al. *Phys. Rev. C* 85:041302 (2012)
127. Lipparini E, Stringari S. *Phys. Rev. C* 175:103 (1989)
128. Trippa L, Coló G, Vigezzi E. *Phys. Rev. C* 77:061304 (2008)
129. Carbone A, et al. *Phys. Rev. C* 81:041301 (2010)
130. Daoutidis I, Goriely S. *Phys. Rev. C* 84:7301 (2011)
131. Reinhard P-G, Nazarewicz W. *Phys. Rev. C* 81:051303 (2010)
132. Danielewicz P, Lee J. *Int. J. Mod. Phys. E* 18:892 (2009)
133. Steiner AW. *Phys. Rev. C* 74:045808 (2006)
134. Hebeler K, Lattimer JM, Pethick CJ, Schwenk A. *Phys. Rev. Lett.* 105:161102 (2010)
135. Gandolfi S, Carlson J, Reddy S. *Phys. Rev. C* 85:032801 (2012)
136. Danielewicz P, Lacey R, Lynch WG. *Science* 298:1592 (2002)
137. Abadie J, et al. *Class. Quantum Gravity* 27:173001 (2010)
138. Bauswein A, Janka H-T, Hebeler K, Schwenk A. *Phys. Rev. D.* In press (2012)

$\underset{R}{A}$

Contents

Indexes

Errata

An online log of corrections to *Annual Review of Nuclear and Particle Science* articles may
be found at http://nucl.annualreviews.org/errata.shtml

ANNUAL REVIEWS
It's about time. Your time. It's time well spent.

New From Annual Reviews:

Annual Review of Statistics and Its Application

Volume 1 • Online January 2014 • http://statistics.annualreviews.org

Editor: **Stephen E. Fienberg,** *Carnegie Mellon University*

Associate Editors: **Nancy Reid,** *University of Toronto*

Stephen M. Stigler, *University of Chicago*

The *Annual Review of Statistics and Its Application* aims to inform statisticians and quantitative methodologists, as well as all scientists and users of statistics about major methodological advances and the computational tools that allow for their implementation. It will include developments in the field of statistics, including theoretical statistical underpinnings of new methodology, as well as developments in specific application domains such as biostatistics and bioinformatics, economics, machine learning, psychology, sociology, and aspects of the physical sciences.

Complimentary online access to the first volume will be available until January 2015.

Access this and all other Annual Reviews journals via your institution at www.annualreviews.org.

ANNUAL REVIEWS | Connect With Our Experts

Tel: 800.523.8635 (US/CAN) | Tel: 650.493.4400 | Fax: 650.424.0910 | Email: service@annualreviews.org